SES6-CT-2005-019757

LARCIS

Large-Area CIS Based Thin-Film Solar Modules for Highly Productive Manufacturing

Specific Targeted Research or Innovation Project
6.1 Sustainable Energy Systems

Publishable Final Activity Report

Draft version!! Still has to be agreed by project partners !!

Date of preparation: 05/02/2010

Start date of project: 01/11/2005 Duration: 48 months

Project coordination: Friedrich Kessler
Zentrum für Sonnenenergie- und Wasserstoff-Forschung
Baden-Württemberg

TABLE OF CONTENTS

1 Project Execution

1.1 Motivation, objectives and contractors involved

In order for the commercial production of large $Cu(In,Ga)Se_2$ based modules on the multi-megawatt scale to be successful, the processes must be streamlined and optimised taking both economical and ecological aspects into consideration. This project aimed to support the development of this material- and energy-saving thin-film technology so it can gain a foothold in the free photovoltaic market. Promising laboratory results are transferred to large-scale production, where the availability of appropriate production equipment and very high material and process yields are of decisive importance. Six universities and research centres and four companies worked closely together in order to merge the physical understanding of the processes and the engineering know-how, both of which are necessary for up-scaling the $Cu(In,Ga)Se_2$ technology to a marketable multi-megawatt production volume.

The overall objective of the project was to develop advanced manufacturing technologies for CIS thin-film solar modules both for the electrodeposition and coevaporation approach. This comprised transfer from laboratory scale to production level.

Goal was to improve the manufacturing techniques for low-cost, stable, efficient and environmentally harmless CIS thin film solar modules on large area. This included work on the molybdenum back contact, the buffer layer, the CIS absorber and the quality and process control. Special emphasis was placed on the development of cadmium-free modules and of electrodeposition methods for CIS absorbers of relevant area. The project structure and consortium was planned to allow the direct transfer of adequate results from the laboratory scale to the operating (pilot) manufacturing plants of Würth Solar (Germany), Solibro (Sweden) and EdF (France).

Summary of main objectives:

- *To develop a high quality back contact on large areas with high adhesion, high conductivity and reduced corrosion by humidity:*

  - To apply additional reflecting TiN and ZrN layers for efficiency enhancement

  - To enhance the stability of the back contact, e.g. by introducing additional layers such as MoX (X = e.g. nitrogen) and ZrN
  - To demonstrate cell efficiencies > 12% with TiN back contact

- *To develop and provide a scalable, cost-effective Cd-free CBD buffer for large areas which is applicable both for the vacuum and the ED CIS approach*

  - To demonstrate devices with CBD deposited ZnS buffer resulting in an efficiency of η >15% (small area), η > 13.5% (30 x 30cm^2) and η > 12% (60 x 120cm^2), respectively

  - To fabricate solar cells with evaporated In_2S_3 buffers and η > 15% (small area)

- *To develop and implement CIS co-evaporation methods which are suitable to enhance module efficiencies on large area in a production line*

  - To fabricate modules with CIS co-evaporation resulting in η >14.5% (30 x 30cm^2) and η > 13.5% (60 x 120cm^2)

  - To build up a graded in-line CIGS co-evaporation process with at least the same efficiencies as obtained with the standard in-line CIS process

- *To demonstrate a working CIS production process by electrodeposition (ED) on an area of 30 x 30cm^2*

  - To fabricate an ED device with $\eta \geq 10\%$ on an area of 30 x 30cm^2

  - To develop and provide a multiple plate reactor for the electrodeposition of CIS up to an area of 30 x 30cm^2; max. efficiency therein: 10%

  - To demonstrate a manufacturing yield of 85% in the 20-plates reactor (30 x 30cm^2)

- *To advance and apply non-destructive process and quality control methods during production and for finished modules*

  - To provide a numerical electronic model for electrodeposited cells and modules which is suitable for device optimisation

  - To identify quality indicators of electrodeposited devices for on-line ED process monitoring

  - To investigate and implement in-situ Raman scattering as monitoring tool for the ED production process

  - To assess the project results regarding achieved yield, material consumption, performance and costs and to benchmark the costs with Si technologies

The contractors involved have been:

1) Zentrum für Sonnenenergie- und Wasserstoff-Forschung Baden-Württemberg (ZSW)
2) Centre National de le Recherche Scientifique (CNRS)
3) Eidgenössische Technische Hochschule Zürich (ETHZ) and Eidgenössische Materialprüfungs- und Forschungsanstalt (EMPA)
4) Helmholtz-Zentrum Berlin (HZB)
5) Univ. Barcelona, Electronic Materials & Engineering (UB-EME)
6) Uppsala University, Ångström Solar Center (UU-ÅSC)
7) Electricité de France (EDF)
8) Saint Gobain Recherche (SGR)
9) Solibro Research AB
10) Würth Solar (WS)

1.2 Project results

1.2.1 Alternative back contact electrodes

Introduction: The objective of this work package was to develop contact electrodes with suitable properties for both electrodeposited and coevaporated absorbers. The properties of the back contact electrode have been found to influence the efficiency of thin film solar cells by e.g. controlling the Na supply to the absorber. It has also been found that one of the weak points of the solar cell is corrosion of Mo back contact electrodes. In the case of damp heat treatments, the Mo electrode corrodes severely and in the case of electrodeposition, the Mo back contact is selenized up to a point which reduces the sheet resistivity of the electrode. In order to reduce both oxidation and selenization of the back contact several strategies were employed. One was to combine Mo with more stable materials such as e.g. TiN and ZrN.

For solar cells with reduced CIGS thickness a strongly reflecting back contact electrode is desirable. Mo is not the best choice in this case, but ZrN has shown promising properties in terms of reflectivity in the wavelength regions of interest. Thus an increased optical length of the solar cell could be expected with use of ZrN as back contact reflector. The effect of increased optical length was also observed in finished solar cell devices using thin CIGS layers, but the ZrN strongly deteriorated the electrical properties of the back contact.

In order to improve the back contact properties in cases with other back contact materials than Mo, a thin layer of molybdenum selenide was used to avoid current transport problems. This thin layer could be obtained with a thin sacrificial layer of Mo, which was subsequently selenized.

TiN as well as ZrN have been found to strongly reduce or even inhibit Na diffusion. Na has therefore to be supplied either by a precursor layer or by a Na post treatment.

1.2.1.1 Enhanced Mo stability

The aim was to improve the stability of the Mo layer against excessive selenization in the thermal annealing step.

The experimental approach was to compare the response to thermal pretreatment in air or argon on the selenization. Two different types of samples were used, one sample with 500 nm thickness with a sheet resistivity of 0.4 ohms/square and one sample with 700 nm thickness with a sheet resistivity of 0.18 ohms/square. These sheet resistivities correspond to 20Ωcm and 13 Ωcm, respectively. The samples are hereafter referred to as high and low resistivity samples, respectively. After selenization of part of the Mo layer, in a process that should correspond to the thermal annealing process the samples were characterized with cross section SEM as well as XRD.

Selenization of the layers without any pre-treatment showed that the high resistivity sample selenized much less than the low resistivity sample. SEM cross sections are shown in Fig. 1.

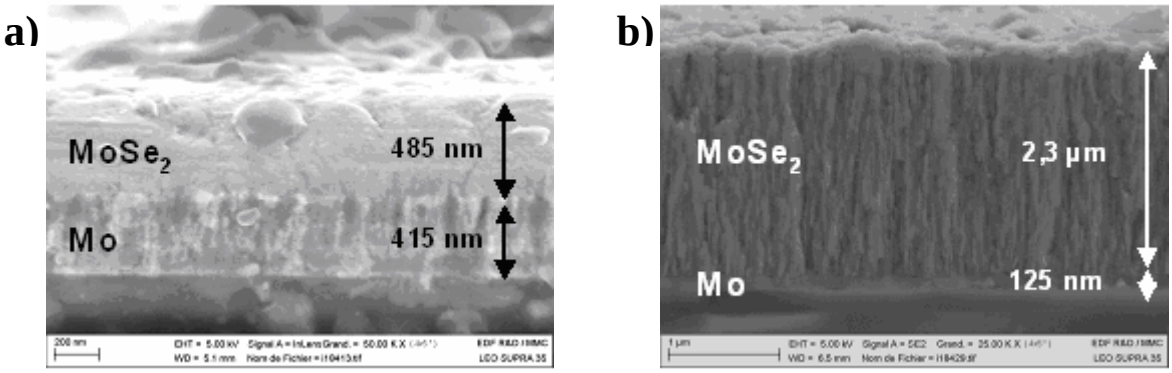

Fig. 1: Cross section of $MoSe_2$/Mo/Glass of SGR500 (a) and SGR700 (b) after selenisation, without thermal pretreatment, observed by FEG-SEM

As can be seen there remains only 125 out of 700 nm of un-selenized Mo in the low resistivity sample, which corresponds to less than 20 %.

The pre-treatment in argon atmosphere reduced the selenization behaviour for both samples, but the low resistivity sample still showed excessive selenization (Fig. 2).

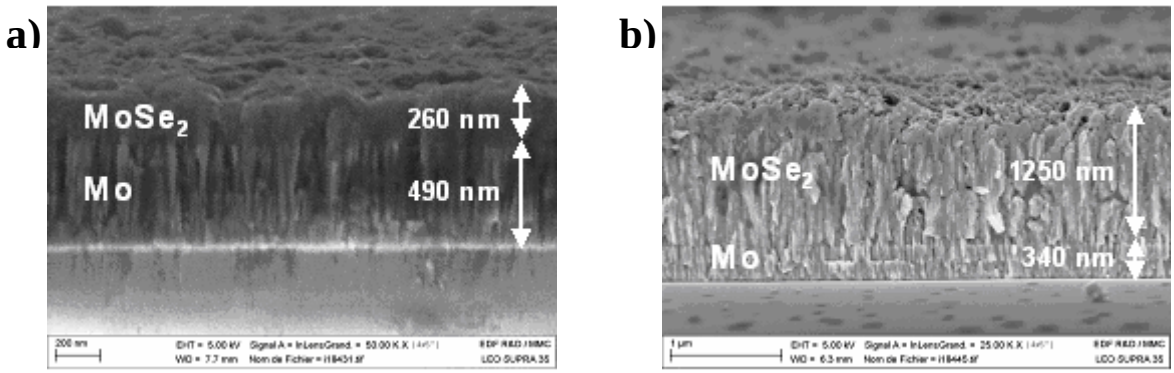

Fig. 2: Cross section of $MoSe_2$/Mo/Glass of SGR500 (a) and SGR700 (b) samples after thermal pretreatment in Ar and selenisation, observed by FEG-SEM

In order to investigate if oxidation of the Mo layer could be important for the selenization behaviour, the second pretreatment was a treatment in air. The result from the air treatment showed that both samples were oxidized, but the low resistivity sample oxidized somewhat less than the high resistivity sample, as shown by XRD. Surface oxide layers could be observed on both samples. The results from the selenization are shown in Fig. 3.

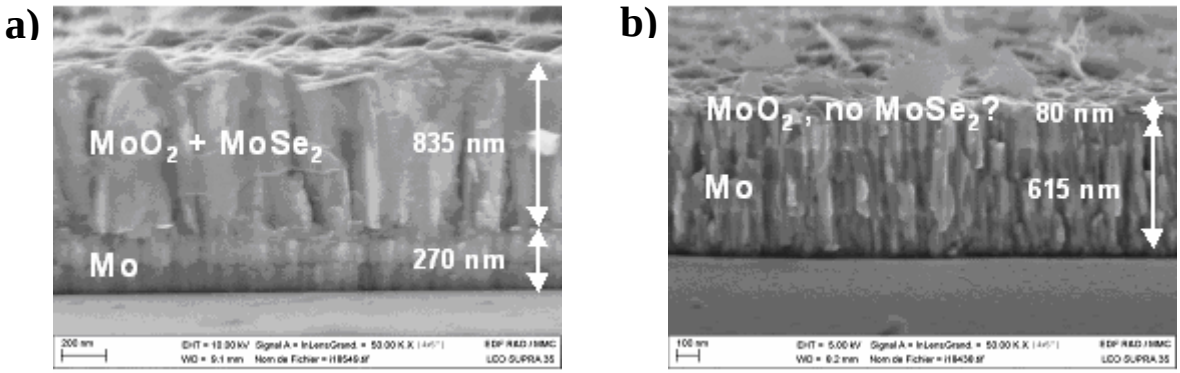

Fig. 3: Cross section of (MoO_2+$MoSe_2$)/Mo/Glass of SGR500 (a) and SGR700 (b) samples after thermal pretreatment in air atmosphere and selenisation, observed by FEG-SEM

In this case there is a dramatic increase in the selenization, but this time only for the high resistivity layer. The low resistivity layer seems to have been protected from selenization by the thin surface oxide, which still was visible after the selenization.

This investigation shows that a reduction of the selenization is possible by optimization of the sputter process and possibly also by using a pretreatment. A high resistivity Mo layer with a high degree of intrinsic porosity is more prone to oxidation, but is less selenized in its as deposited or argon annealed state. A low resistivity Mo layer with a more closed structure is much more severely selenized in its un-annealed or Ar annealed state. However oxidation of the surface layer reduces the selenization substantially, leaving the oxide almost intact.

1.2.1.2 TiN and ZrN as back contact

In order to investigate the Mo pre-selenization and the effect of a Mo/Se layer interface at the solar cell back contact CIGS solar cells on soda lime glass substrates with TiN and ZrN back contacts were processed. Both kinds of back contacts were deposited using reactive DC sputtering method. The TiN-layers were deposited by SGR and the ZrN-layers by UU-ASC. On some samples a thin (10nm) Mo film was deposited with dc sputtering on top of the TiN. In some cases this thin Mo layer was converted into $MoSe_2$ by the Se-furnace method. With this method the conversion of Mo into $MoSe_2$ could be clearly demonstrated.

The CIGS absorber layers were grown using the 3-stage process (ETHZ/EMPA). It was found that the deposited nitrides act as diffusion barrier for Na. Therefore sodium was added to the absorber with a post-deposition treatment (PDT). Since the PDT shows the best performance for CIGS layers deposited at temperature in the range of 400 - 500°C, all samples were grown at maximum temperature of 450°C. The solar cells were completed by depositing CBD-CdS buffer, RF sputtered ZnO:Al/i-ZnO and a Al/Ni-grid.

One task of project work of ETHZ/EMPA aimed to investigate the Mo pre-selenization and the effect of a Mo/Se layer interface at the solar cell back contact.

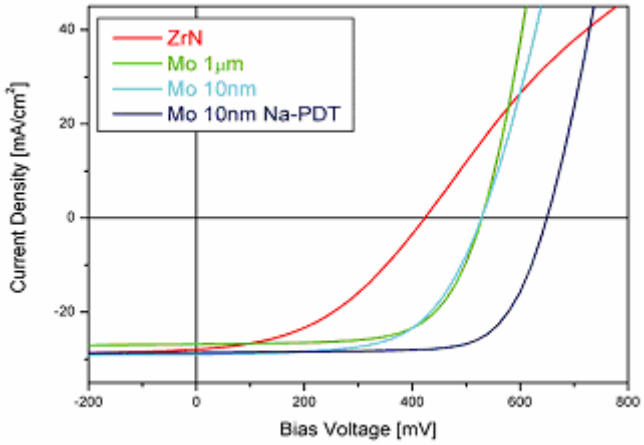

Fig. 4: IV-curves of CIGS solar cells with ZrN back contacts and intermediate Mo layers

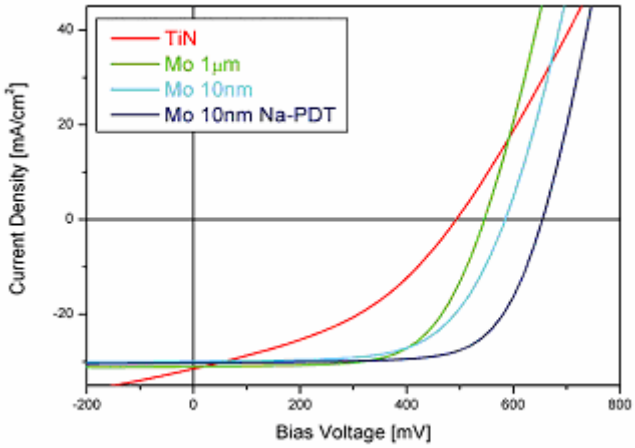

Fig. 5: IV-curves of CIGS solar cells with TiN back contacts and intermediate Mo layers

I-V curves of samples with ZrN and TiN back contact are shown in Fig. 4 and Fig. 5, respectively. It was found for both cases, that a thin Mo-layer is required to achieve good cell efficiencies. The presence of the Mo layer seems to be essential to get higher V_{OC} and FF, as can been seen by comparing the cells grown directly on the nitrides with those with additional Mo-layer. This is due to the formation of $MoSe_2$ at the interface, which ensures ohmic contact to CIGS layer. Results have shown that even a thin Mo-layer of ≈ 10 nm is sufficient to ensure same photovoltaic properties as with "usual" thicknesses.

Tab. 1: Overview of obtained results (low temperature process, T_{max} = 450°C)

Back contact	**V_{OC} (mV)**	**J_{SC} (mA/ cm^2)**	**FF (%)**	**η (%)**
ZrN	599	27.9	57.4	9.4
ZrN + 10nm Mo	649	29.3	72.5	13.9
TiN	493	31.5	39.8	6.2
TiN + 10nm Mo	655	30.3	69.7	13.8

1.2.1.3 ZrN as back contact reflector layer

In a solar cell with *thin* CIGS layer two major losses are observed: The first is absorption loss (especially) in the infrared region of the spectrum, where the absorption coefficient is low. For CIGS layers with a thickness below e.g. 1 µm, these losses are significant. In order to reduce them a back reflector layer can be used to reflect non-absorbed photons back into the absorber in order to become re-absorbed. The other major loss is due to recombination at the back contact since in a solar cell with thin absorber a significant fraction of the electrons comes from a region close to the back contact. Therefore the recombination properties at the back contact are of big interest.

ZrN is a promising candidate as reflecting layer since the sputtering rate can be rather high and since it has good reflective properties.

Results and assessment: Stoichiometric samples had the highest conductivity and were most reflecting in the infrared. Above 800 nm about 60 % reflectance was obtained at the back contact-to-CIGS interface, which is three times higher than the Mo reflectivity. However, in order to obtain a good ohmic contact a thin Mo layer was required. This Mo layer had to be fully selenized in order to be transparent enough for the ZrN to be useful in terms of using its reflectivity. A thin $MoSe_2$ layer also gave a good ohmic contact.

The assessment of investigation was that even though good reflective properties could be obtained for a ZrN layer, the losses, both electrical losses as well as optical could not completely be avoided. Calculations performed in another work package regarding the influence of efficiency for the cost structures in CIGS solar cell modules gave clear indications that the addition of an extra layer together with a small loss in efficiency could not make up for the reduction in CIGS material cost and increased throughput in the CIGS deposition step.

1.2.1.4 New cost-effective back contact electrodes

In order to keep the ohmic losses as low as possible and for homogeneous electrodeposition of absorbers on large area glass substrates the conductivity of an alternative back contact should be as high as possible. On the other hand, the costs should not be higher than standard Mo electrodes. To meet all requirements SGR pursued the following strategies:

- To reduce the Mo thickness to 20 – 30 nm to assure an ohmic contact
- To substitute the Mo layer by a cheaper metal like Cu or Al
- To avoid diffusion of undesired elements like Cu by thin TiN or ZrN diffusion barriers

Stacks of e.g. glass/TiN/Mo, glass/Ti/Cu/TiN/Mo, glass/Ti/Cu/TiN and glass/Ti/Mo with different resistances and thickness were sputtered by SGR and forwarded to the other partners.

Results achieved with coevapored absorbers at UU-ASC and ZSW on these new back contacts were promising on the one hand, since devices of more than 11% could be made (see Fig. 6. On the other hand, however, reference results were clearly better both in efficiency (e.g. 11.6% compared to 13.4%) and especially yield. A challenge (amongst others) arose from the patterning of the back contact (P1): the absorber layer did not adhere in the P1 patterning line where the back contact was removed. Furthermore, diffusion of undesired elements into the absorber occurred. The TiN layers were effective barrier layers both for the copper and the sodium diffusion. For the final assessment of the new back contacts more work has to be done, especially regarding Na provision, film adhesion and patterning which exceed the purpose of this project.

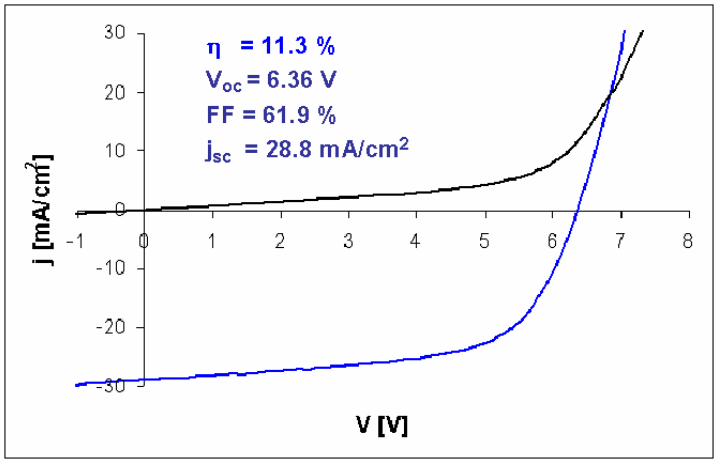

Fig. 6: IV-curve of a monolithically integrated module with ten cells in series on the back contact structure Ti/Cu/TiN/Mo

1.2.2 Alternative buffer layers

Introduction: The first aim of this task was to develop a chemical bath deposited (CBD) ZnS-based buffer layer for large area modules up to 60×120 cm^2 area that is applicable on both evaporated and eletrodeposited $Cu(In,Ga)(Se,S)_2$ (CIGS) absorbers layers. The priority for industrial applications was to achieve a scalable, easy controllable CBD process, which is characterized by a short deposition time t<10min and a limited number of precursor chemicals so that the process can be easily adapted in already commercial available CBD systems. Other

limitations given by the industrial contractors within the project were to realize module devices with conversion efficiencies comparable or even higher as with the traditional used CdS buffer, which achieve their maximum performance without any intermediate- and post-annealing or light-soaking steps and which demonstrate excellent long-term stability behaviour by accelerated life-time-testing.

To meet this intensions the normally used undoped high-resistivity ZnO interlayer in CIGS-based devices was additionally replaced by a high-resistivity ZnMgO layer. One objective was to achieve high-efficient and stable small area cells by defining a [Mg]/([Mg]+[Zn]) ratio for optimal band alignment and sputtering parameters for reduced interface damage. Another objective was to scale up the process from a static deposition on small areas to a dynamic in-line deposition on 30×30cm^2 and later on 60×120cm^2 substrates using thereby linear ceramic ZnMgO cathodes. This should result to η >13.5% efficient co-evaporated CIGS 30×30 cm^2 modules and to η >12% efficient co-evaporated CIGS 60×120 cm^2 modules.

The other aim was to investigate an alternative vacuum In_2S_3 buffer layer by applying the compound evaporation method and to fabricate small area solar cells with an efficiency of η >15%. This included the detailed examination of the influence of the annealing process on the device characteristics determining the approximate Cu content inside the buffer layer at optimum device performance by means of x-ray photoelectron spectroscopy (XPS) and energy dispersive X-ray spectroscopy (EDX). It also included a closer look at the annealing-induced changes of the electronic device properties and the recombination behaviour.

1.2.2.1 Cd-free CBD-buffer on large area

The limitations given by the industrial partners were taken in to account for further investigations in this project. For that, and in order to minimise the reproducibility problems and insufficient long-term device stability both the CdS and i-ZnO layers were replaced by CBD ZnS and $Zn_{1-x}Mg_xO$ as shown in Fig. 7. CNRS/IRDEP has specially studied the optimisation of short time (t<10 min) CBD ZnS deposition and ZSW the optimisation of the ZnMgO layer by sputtering

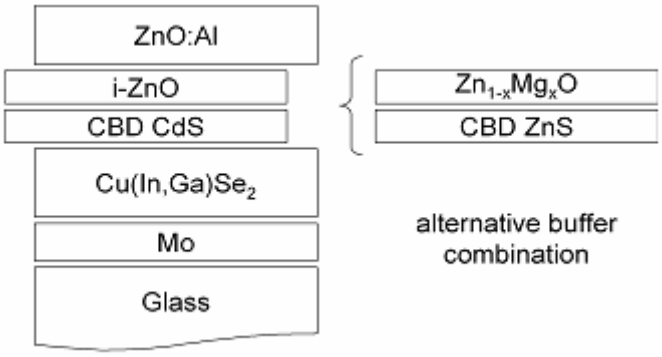

Fig. 7: Schematic view of the CIGS solar cell structure substituting the CdS/i-ZnO layers by ZnS/$Zn_{1-x}Mg_xO$

The goal of CNRS/IRDEP was to develop a bath CBD-ZnS formulation using maximum four chemicals, leading to a deposition time lower than 10 min. During this project, a simple way to reduce the deposition time of the ZnS buffer layer without major change in the formulation

of the chemical bath was developed. Firstly, the influence of the deposition temperature was studied theoretically by constructing solubility diagrams of ZnS, ZnO, and $Zn(OH)_2$ as a function of pH and temperature. In situ growth deposition studies were carried out by quartz microgravimetry (QCM) as a function of deposition parameters. These studies allowed us to reduce the deposition time below 10 min improving thereby the deposition conditions for obtaining dense and covering films. In fact, in the standard CBD deposition, the reagents were mixed at room temperature, added in the deposition reactor, and heated. We observed by this standard procedure that the focused deposition temperature (for example 80 °C) is reached only after more than 10 minutes (i.e. 15 minutes up to 80 °C), which can slow down the overall deposition rate.

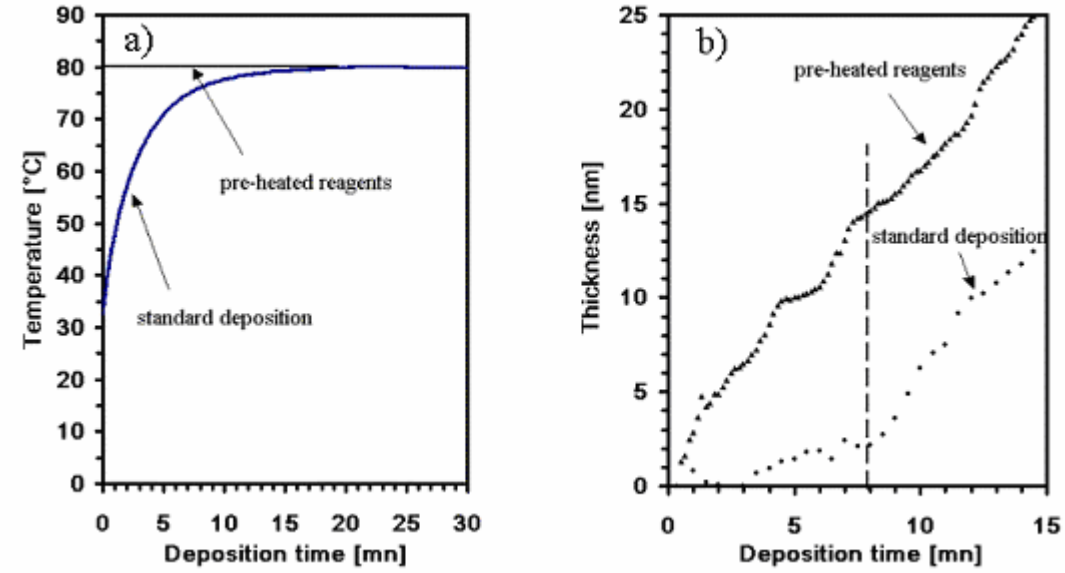

Fig. 8: (a) Variation of the temperature of the CBD bath as function of deposition time of a standard Zn(S,O,OH) and (b) comparison of QCM growth rate plots of "standard" and "pre-heated" Zn(S,O,OH) thin films.

To avoid this problem, the reagents were pre-heated before starting the deposition. Once the deposition temperature is reached for all reagents, they were mixed together and added to the also preheated deposition reactor. This allowed reducing significantly the heating time ramp (Fig. 8). The optimized short time deposited CBD-ZnS buffers were then tested on several co-evaporated $Cu(In,Ga)Se_2$ (CIGSe) layers and electrodeposited $CuIn(S,Se)_2$ (ED-CIS) layers. Efficiencies similar or even better than those with CdS buffer layer were obtained for ED-CIS and CIGSe respectively (8.5% and 15.7%). Finally, the homogeneity and reproducibility of these depositions on 5×5 cm^2 samples have been studied (Fig. 9).

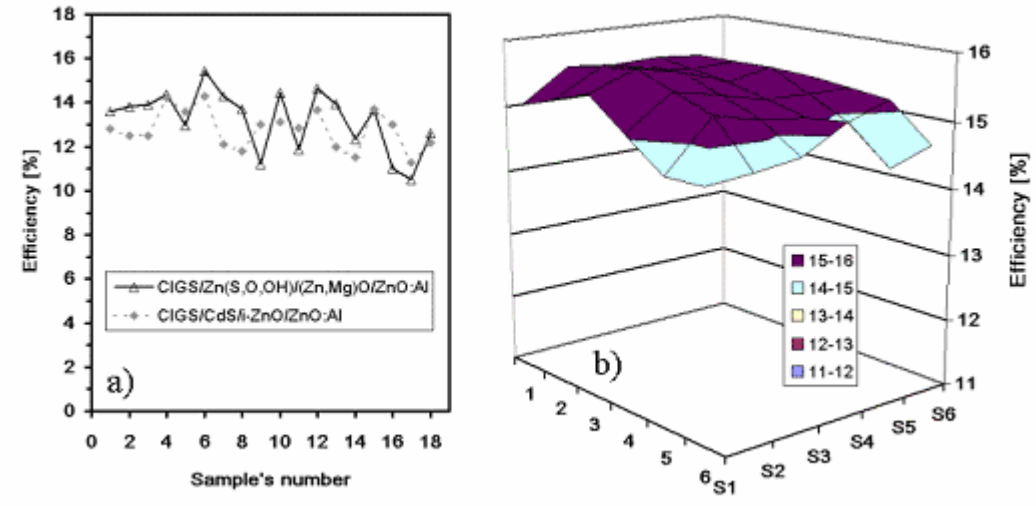

Fig. 9: (a) Reproducibility of cell efficiencies with pre-heated Zn(S,O,OH)/(Zn,Mg)O buffer layer for CIGSe absorbers on eighteen 2.5×2.5 cm^2 cells in comparison to CdS/i-ZnO buffer layer and (b) homogeneity of efficiencies on a surface of 5×5 cm^2 with pre-heated Zn(S,O,OH)/(Zn,Mg)O buffer layer

Based on QCM measurements a growth mechanism controlled by chemical reactions and independent of the stirring rate has been determined. It was shown that the deposition mechanism seems to be a surface reaction, limited kinetics explaining the low dependence on the hydrodynamic regimes. Based on theoretical solution chemistry considerations by constructing solubility diagrams of ZnS, ZnO, and $Zn(OH)_2$ as a function of temperature and XPS measurements at different deposition times, it was shown that under these conditions and in the first stage of deposition it is not possible to avoid the presence of ZnO and $Zn(OH)_2$ in the films. A typical CBD Zn(S,O,OH) layer on CIGS used as buffer layer in solar cell devices is shown in Fig. 10.

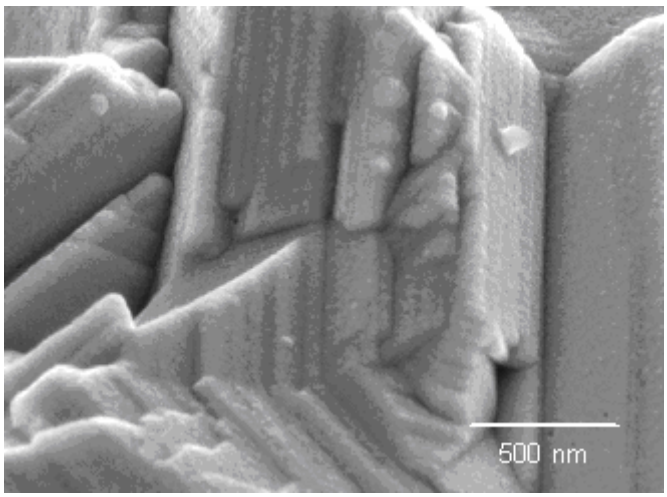

Fig. 10: SEM top view image of a 30 nm CBD Zn(S,O,OH) film on CIGS

In parallel, in order to reduce the transient behaviour observed by the Zn(S,O)/i-ZnO buffer combination and to stabilise the cells on a high efficiency level, ZSW started experiments

replacing i-ZnO by a ZnMgO layer. The ZnMgO film was deposited by rf-sputtering using ceramic targets. In order to achieve an optimal band alignment, the [Mg]/([Mg]+[Zn]) ratio in the layer was varied by using different ZnMgO targets with different Mg concentrations. Sputtering at lower power densities was found to be important for reduced sputter damage. Improved heterojunctions with a high efficiency level and a good reproducibility were demonstrated. Due to the higher transmission of the Zn(S,O)/$Zn_{1-x}Mg_xO$, layers in the spectral region between 330 and 550 nm as compared to CdS/i-ZnO, a large gain in short-circuit current density was obtained, leading to a higher conversion efficiency. At Mg concentrations between 15 and 26 % in the $Zn_{1-x}Mg_xO$ layer the devices prepared under optimized conditions demonstrated the highest efficiencies. Furthermore, a strong reduction of transient effects and enhanced stability against damp-heat conditions and thermal impact were observed. Small-cell efficiencies of 18.0 % and 10×10cm^2 module efficiencies of 15.2 % were realized using in-line multi-stage CIGS absorber layers (Fig. 11).

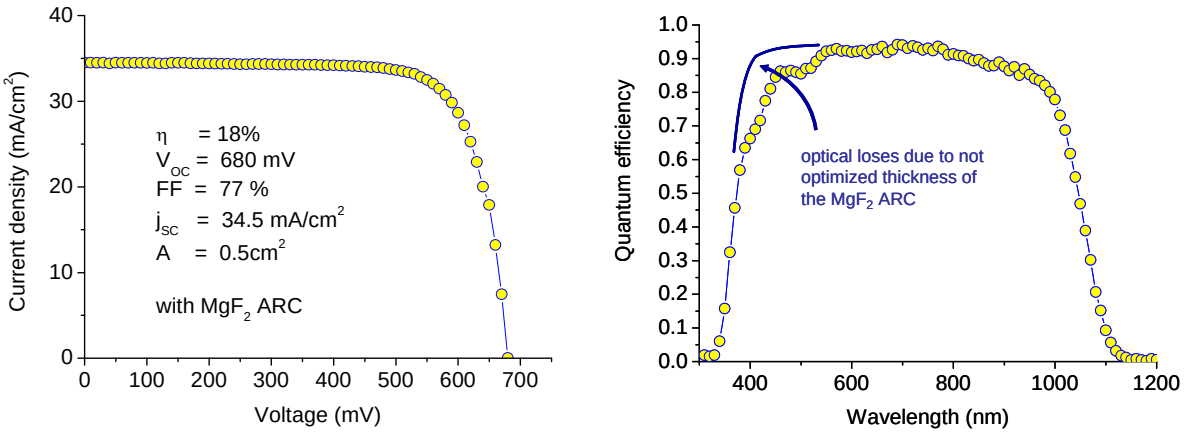

Fig. 11: (a) Current-voltage characteristic under simulated AM1.5-100mW/cm^2- illumination and (b) spectral response of the best CIGS cell with a ZnS/ZnMgO buffer layer and MgF_2 anti-reflection coating

By studying the impact of heat treatment and light soaking effects relying on a detail comparison of the properties of these different layers and of their combination, it was noted that for CIGS/CBD-Zn(S,O,OH)/rf-ZnMgO/ZnO:Al cells the post-treatments only affect the fill factor. On the contrary, for CIGS/CBD-Zn(S,O,OH)/i-ZnO/ZnO:Al the Voc also varies.

The final objective of this work package was the up-scaling of CBD-Zn(S,O) to ≥ 30×30 cm^2 surfaces and the optimization of magnetron sputtering of the $Zn_{1-x}Mg_xO$ layer in the dynamic mode of large area applications (≥ 30×30 cm^2). At this stage it was observed that during the up-scaling to large areas of the CBD Zn(S,O) film growth, uncovered areas are present on CIGS surface. A very close collaboration between CNRS and ZSW for the last period of LARCIS project led to develop a homogeneous covering of Zn(S,O) buffer layer for 30×30 cm^2 absorbers. A 30×30 cm^2 module with an efficiency of 12.9% and a fill factor of 70.9% was obtained (Fig. 12).

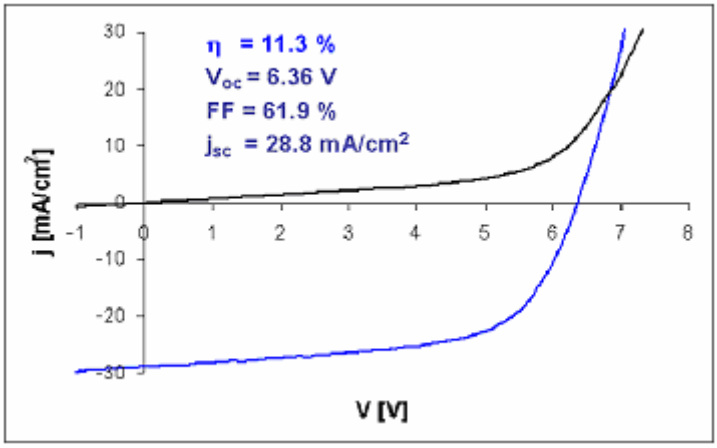

Fig. 12: IV Characteristic of the best 30 × 30 cm² CIGSe module with ZnS/ZnMgO buffer

The CBD ZnS process developed at IRDEP/ZSW was tested at the Würth Solar (WS) production line on 60×120 cm² absorbers. Due to different machine geometry, the CBD ZnS process was modified and adapted to the WS facility conditions. Homogeneity tests were performed. The ZnS thickness homogeneity was examined by SEM measurements. The efficiency homogeneity over the 60×120 cm² substrate area was analysed on 30×30 cm² segments, which were cut from the 60×120 cm² substrate. The completion of these segments to module devices with ZnMgO buffer and ZnO:Al TCO as well as the electrical characterisation were performed at ZSW. The efficiency level on 30×30cm² modules cut from a 60×120 cm² substrate was limited in the range of $\eta \approx 10$ - 12% that was mainly influenced by the fill factor due to shunting problems. Probably, the imperfect ZnS coverage could be one of the reasons. The device parameters of the best 30×30cm² module cut from a 60×120 cm² substrate after post-anneal and post-light-soak were $\eta = 12.3\%$, $V_{OC} = 40.04$ V, FF = 69.84%, $I_{SC} = 320$ mA (j_{SC}=28 mA/cm²).

The earlier-than-planned doubling of production capacity at WS in 2008 led to the problem that the ZnO sputter system was not available for ZnMgO sputtering on 60×120cm². So, although good progress was made with CBD ZnS deposition, 60×120cm² substrates could not be processed further in the production line. ZnMgO large-area sputtering capacities at WS will be available from Nov 2009 onwards and first complete 60×120 cm² Cd-free modules are expected at the end of 2009.

1.2.2.2 In_2S_3 by evaporation

The objective of this work package was to fabricate solar cells with evaporated In_2S_3 buffer layers and efficiencies of >15%. The main task comprises an investigation into the prerequisites for large-area deposition in industrial production.

Tab. 2: Optimised standard process parameters for the In_2S_3 buffer layer deposition.

In_2S_3 buffer layer deposition		Post deposition annealing	
chamber base pressure	< 5×10^{-5} mbar	annealing temperature	200°C
crucible temperature	720 °C	annealing time	35-55min
substrate temperature	< 50 °C	atmosphere	in air
buffer layer thickness	50 nm		

In a first step, the buffer layer deposition process parameters had to be optimised in view of optimal device performance. Some of the optimised standard deposition parameters are summarised in Tab. 2. We found strong variations in the quality in terms of purity, stoichiometry and crystallinity in commercially available In_2S_3 powders. The quality of the In_2S_3 powders used for the evaporation process ultimately determines the quality of the In_2S_3 buffer layer and best solar cell efficiencies were found for a highly pure, single phase, crystalline In_2S_3 source material.

Single phase In_2S_3 source material was found to be stable during the deposition process and could be used during multiple deposition runs. Resulting In_2S_3 thin films were stoichiometric and homogeneous with an indirect optical band gap of (1.99±0.5) eV.

The utilisation of crystalline, single phase source material and the development of appropriate buffer processing led to high efficiency solar cells. A key process for optimal device performance was post deposition annealing of the completed solar cells for 35min. to 55min. at a temperature of 200°C. Annealing was found to improve mainly the fill factor and open circuit voltage of devices with In_2S_3 buffer, independent of the atmosphere in which the annealing was carried out (e.g. in air or inert gas). The controlled and reproducible enhancement of the device performance during annealing allowed coherently analysing the changes in the photo-generated charge carrier collection and the dominant recombination mechanism of the solar cell devices. Losses in the spectral response upon annealing observed at long wavelengths (700-1200 nm) were attributed to a reduction of the space charge region width at the In_2S_3/ Cu(In,Ga)Se_2 junction.

The recombination of charge carriers could be reduced by the annealing and the dominant recombination mechanism gradually changed. Prior to annealing, it was shown to have a high tunnelling contribution (diode quality factors of up to 6) and was associated with a mechanism located at the In_2S_3/ Cu(In,Ga)Se_2 interface. In annealed devices, it was attributed to a thermally activated recombination in the space charge region. As a result of the reduced recombination the open circuit voltage of the ZnO/ In_2S_3/ Cu(In,Ga)Se_2/Mo devices could be reproducibly increased upon annealing by 100-150 mV and devices were fabricated with open circuit voltages beyond those of the established CdS/ Cu(In,Ga)Se_2 reference cells. Thus, the potential of In_2S_3 to form high quality junctions with Cu(In,Ga)Se_2 could be demonstrated.

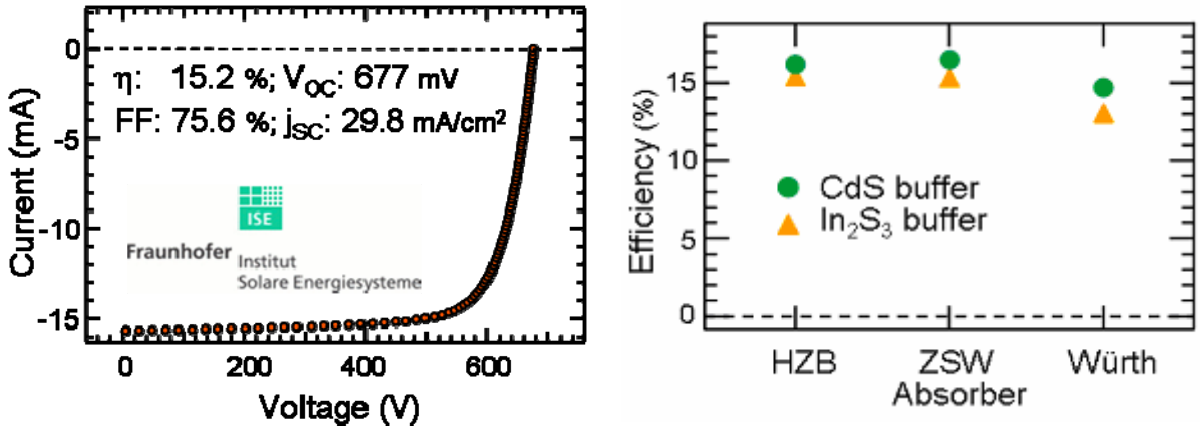

Fig. 13: Left: IV-characteristics of a device with an evaporated In_2S_3 buffer layer as independently confirmed by Fraunhofer ISE, Freiburg, Germany (total area efficiency, device with AR). Right: Efficiencies of the best cells achieved with evaporated In_2S_3 buffers on different absorbers (after annealing for 35-45 min. at 200°C) and their corresponding CdS references (total area efficiencies, no AR).

By a combination of bulk and surface sensitive analysis methods, a pronounced Cu diffusion from the $Cu(In,Ga)Se_2$ absorber into the In_2S_3 layer could be shown as a result of the annealing. In_2S_3/ $Cu(In,Ga)Se_2$-bilayer structures were analysed by: (1) high kinetic energy X-ray photoelectron spectroscopy (HIKE) probing the integral Cu signal of Cu in the In_2S_3 layer, (2) standard X-ray photoelectron spectroscopy (XPS) detecting the increasing Cu content at the In_2S_3 surface and (3) energy-dispersive X-ray spectroscopy (EDX) measuring the Cu distribution in the In_2S_3 layer. All methods gave a clear proof that Cu diffuses into the In_2S_3 and indicated a solubility limit of 4-9 at.% for Cu in In_2S_3.

Based on the developed buffer processing new record efficiencies for $Cu(In,Ga)Se_2$ solar cells with an evaporated buffer layer could be obtained. The calibration laboratory of the Fraunhofer Institut für Solare Energiesysteme, Freiburg, has confirmed record cell efficiencies of (15.2±0.1)% (FF= 75.6%, j_{SC}= 29.8 mA/cm^2, V_{OC}= 677 mV), see *Fig. 13*, left. High efficiency devices with In_2S_3 buffer layer could be obtained on different $Cu(In,Ga)Se_2$ absorber types with efficiencies comparable to their CdS counterparts (*Fig. 13*, right). The still small gap between In_2S_3 buffered devices and their CdS counterparts is mainly due to a loss in the short circuit current as mentioned earlier.

The high potential of evaporated In_2S_3 buffer layers in an industrial process could be shown and the ability to form high efficiency devices and high quality junctions has been demonstrated. However, some obstacles still have to be addressed in view of an industrial implementation which mainly concerns the current collection and the cycle time.

Tab. 3: Cell parameters for the best device obtained with an evaporated In_2S_3 buffer layer (ZnO/ (50nm) In_2S_3 / (HZB) $Cu(In,Ga)Se_2$ / Mo) and its corresponding CdS reference device.

Buffer	η	FF	V_{OC}	j_{SC}
Evap. In_2S_3	15.4 %	72.7 %	628 mV	33.7 mA/cm^2
CBD CdS	16.2 %	74.4 %	639mV	34.0 mA/cm^2

1.2.3 Evaporated CIGS absorbers

Introduction: The overall objective of this task was finding a suitable method for the reduction of production costs for the industrial production of large area modules (120 x 60 cm^2).

In order to achieve this goal, two main approaches have been investigated. These were the reduction of CIGS related material costs and the improvement of device efficiency by the improvement of the CIGS evaporation process.

Three research institutes (ZSW, EMPA, UU-ASC) and two industrial partners (Würth Solar, Solibro) that produce large area CIGS modules contributed to this effort.

In the beginning all three research institutes invested a lot of work in the reduction of CIGS material costs by using thinner CIGS layers. This approach required the development of appropriate solutions for the losses that accompanied such a reduction of the CIGS absorber thickness. UU-ASC investigated a solution that purposed to use reflectors at the back of the thinned CIGS absorber in order to facilitate a complete absorption of the sun´s light. EMPA followed another approach that omits the following buffer layer process completely, which obviously cuts cost but also poses a particular challenge for junction formation in the

semiconductor. Solibro investigated the dependence of a varying CIGS absorber thickness versus device efficiency in an industrial environment.

An alternative approach to cost effective large area CIGS production was the enhancement of module efficiency by the optimisation and transfer of high efficiency lab processes to an industrial environment. All research partners experimented with a graded CIS process. UU-ASC and EMPA have supported this move by investigating specific features of the graded absorber process in order to increase its potential. ZSW has ventured into transferring the graded process to a pre-production inline CIS deposition system.

Both industrial partners together with the research institutes evaluated the results of both approaches on the basis of a realistic production cost scenario. In the end the most cost effective approach was determined.

1.2.3.1 Thin CIGS

Back-reflector

In order to study the influence of CIGS thickness on solar cell module parameters a series of solar cell modules was prepared. CIGS layers with varying thickness from 550 nm up to 1.2 µm were used. An SEM image of the structure is shown in Fig. 14. The relative depth of the back contact graded layer was kept constant independent of the total thickness. In Tab. 4, the results are listed.

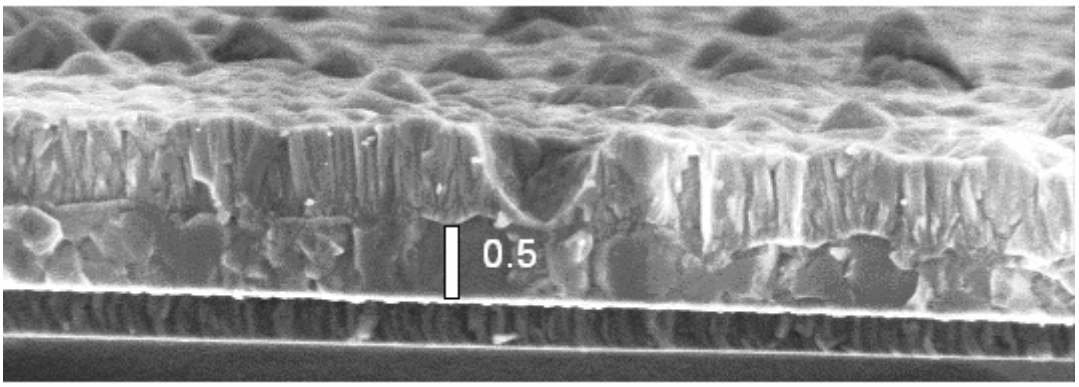

Fig. 14: An SEM image of a reference device from thin module CIGS run. The thickness of the CIGS layer is indicated by a white bar. The ZnO thickness is the normal thickness for solar cell devices. For modules the doped ZnO is twice the thickness used for cells.

Tab. 4: The first module series using extremely thin CIGS layers. Some of the modules suffered from shunting. The module size is 5 x 5 cm^2

thickness	Voc/cell	Jsc	FF	eff
0.55	607	23.5	69	9.9
0.56	561	23.0	68.3	8.8
0.74	650	23.4	70.3	11.0
0.87	620	25.2	68.8	10.8
1.1	572	27.6	56.4	8.8

As can be seen the fill factors of the modules are relatively independent of thickness for these modules. As expected the current density decreases with thickness. A QE analysis of reference solar cells using the same CIGS absorbers as the modules at 0.55 and 0.87 µm, respectively, is showed in Fig. 15.

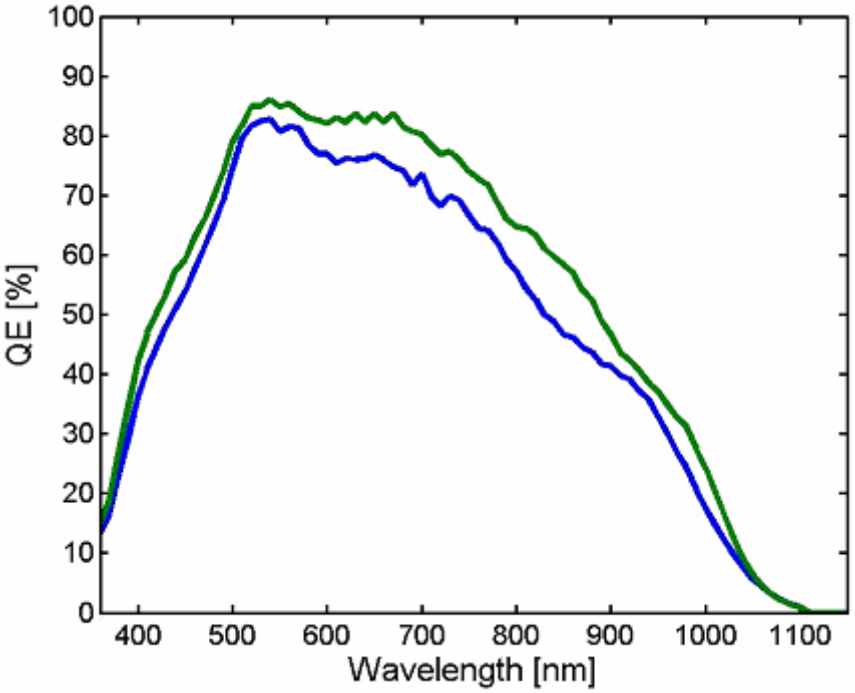

Fig. 15: Quantum efficiency analysis of two reference cells from the module series. The CIGS thicknesses were 0.55 (blue line) and 0.87 (green line) respectively

In order to reduce the current loss, some modules were prepared on ZrN back reflector coated Mo/glass substrates. The results: Na diffusion through the scribe lines led to severe shunting of the modules and no efficiency could be measured. A typical example of a scribe line is shown in Fig. 16. As can be seen, uncoated ZrN is visible through the ZnO and there is electrical contact between the doped ZnO and the ZrN-coated back contact on both sides of the scribe, effectively shorting the individual cells of the module.

The problem of CIGS adhesion and growth problems using substrate materials with a low diffusion coefficient for Na (e. g. Mo/glass where the Mo has low diffusivity for Na) has been observed before with our inline CIGS process. The problem is not the limited Na diffusion itself, but presence of pinholes where Na can diffuse freely into the CIGS. A scribe can be described as a giant pinhole and thus excessive Na diffusion will take place there. The problem is much smaller in the case of the graded absorber process. Therefore it might be preferable to change the CIGS process to the graded process in order to be able to use Na tight materials such as ZrN. The lack of Na during the growth of the CIGS layer results in inferior electrical properties of CIGS but with the use of the post deposition treatment with Na the CIGS material quality could most likely be restored to about the same level as when Na is present during growth.

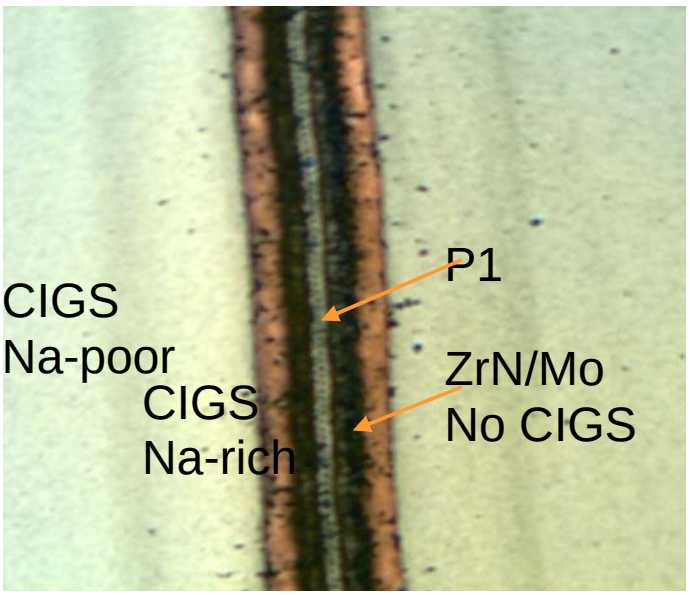

Fig. 16: A scribe in a module with ZrN back contact reflector as observed in an optical microscope. The light grey areas are coated with CIGS. In the vicinity of the scribe there is a slight colour change indicative of increased Na content. Close to the scribe the ZrN is visible without a CIGS coating and in the middle the P1 scribe can be seen.

Using a moderately thin CIGS layer of 1.6 µm, the best efficiency obtained is 13.1 % for a small module (12.5x12.5 cm).

Optical characterization and modelling of CIGS structures specially designed for this purpose was made in a separate collaboration with the University of Ljubljana. It was found that at 360 nm thick CIGS layers (the thickness of the specially designed samples) up to 9 % improvement of the current could be achieved. At larger CIGS thickness the relative improvement would be smaller. The net gain of a back contact reflector on the short circuit current for a cell with a CIGS layer of 1.5 µm thickness would be less than 1 %.

The current density for the cells prepared with 360 nm CIGS was about 22.5mA/cm^2. A 9 % relative improvement of the current density would lead to 24.5mA/cm^2. This is substantially less than about 30mA/cm^2 which is normally achieved for a CIGS thickness of 1.5 µm.

A nine percent improvement of the current density of the thinnest module, in our case with 0.5 µm thick CIGS, would lead to an efficiency increase from 9.9 to 10.7 % with a current gain from 23.5 to 25.6 mA/cm^2. The current loss in the former case, as compared to 1.5 µm CIGS, is 22 % and in the latter with the reflector it would be reduced to 15 %, i.e. less than one third of the current loss is avoided.

Modified CIGS absorber for buffer-free cells

The aim of the work was to develop a process of absorber layer modification that avoids the separate deposition of a buffer layer while that usually maintains high efficiency in CIGS solar cells. The process should be compatible to in-line production and should enable to reduce both processing time and manufacturing costs.

In order to avoid the additional buffer layer deposition the finishing of the CIGS deposition process has been modified. After a standard CIGS growth process the samples were cooled down to approx. 200˚C and a thin layers of $In_xGa_{1-x}Se_y$ with thicknesses of ≈10 nm were

subsequently evaporated. Fig. 17 shows best cell results compared to reference result obtained with an In_xS_y buffer layer, deposited by ultrasonic spray pyrolysis (USP).

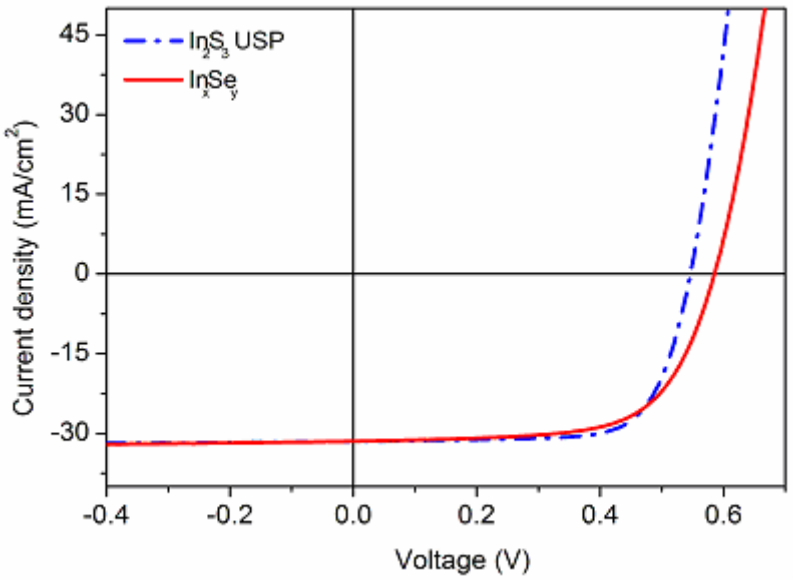

Fig. 17: IV-curves of solar cells with a 10 nm thick In_xSe_y finishing (solid red line) compared to an alternative In_2S_3 buffer layer, deposited by ultrasonic spray pyrolysis (USP). Both cells included an antireflection coating.

With the additional application of a ≈10 nm thick indium selenide layer deposited directly after CIGS processing a 12% efficient solar cell has been obtained. The electronic properties of processed cells are comparable to cells with alternative In_2S_3 buffer layer. However, only efficiencies in the range of 1-2 % below those achieved with standard manufacturing techniques can be obtained up to now.

Absorber thickness versus device performance – cells and submodules (Solibro AB)

A number of CIGS depositions have been made with different thickness of the CIGS layer. The CIGS layers have been used to fabricate small test cells (total area 0.5 cm^2) as well as submodules (substrate size 27.5 x 30 cm^2). The overall result is exhibited in Fig. 18. It can be seen the thickness influence on device performance is quite week over the thickness interval 1.1 - 2.0 µm. This differs from the expectations of a much stronger efficiency loss when the thickness is reduced below 1.5 µm related to the loss of light absorption at low absorber layer thickness.

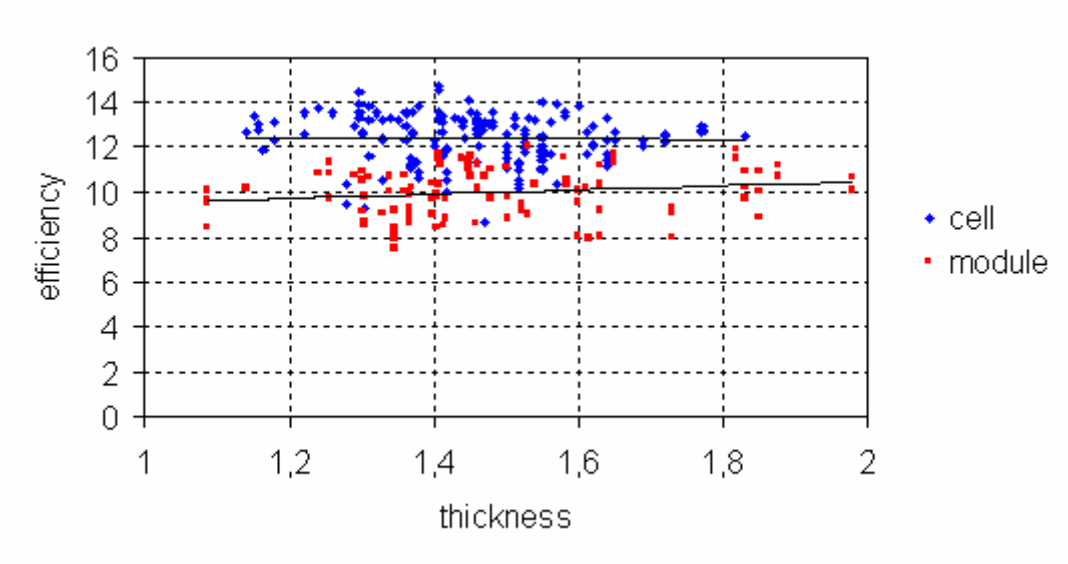

Fig. 18: Cell and module efficiency as a function of CIGS absorber thickness

By looking at the short circuit current of the devices, the interdependency of thickness and light-induced current, the effect of reduced absorption at low thickness can be clearly seen. This effect is counterbalanced by an increased voltage at lower thickness, the fill factor being essentially constant with absorber thickness. The corresponding current and voltage data is displayed in Fig. 19 and Fig. 20.

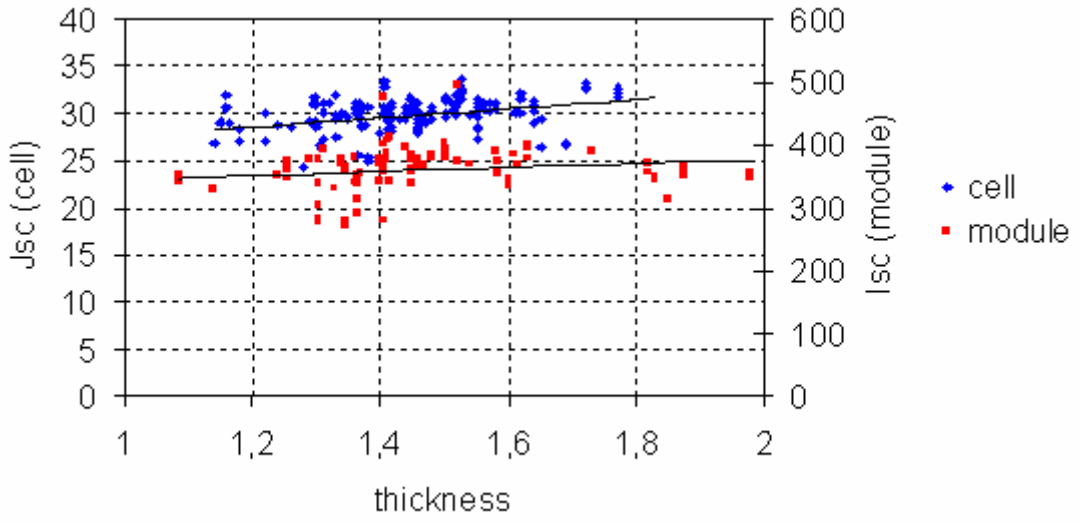

Fig. 19: Short circuit current of cells and submodules as a function of CIGS absorber thickness

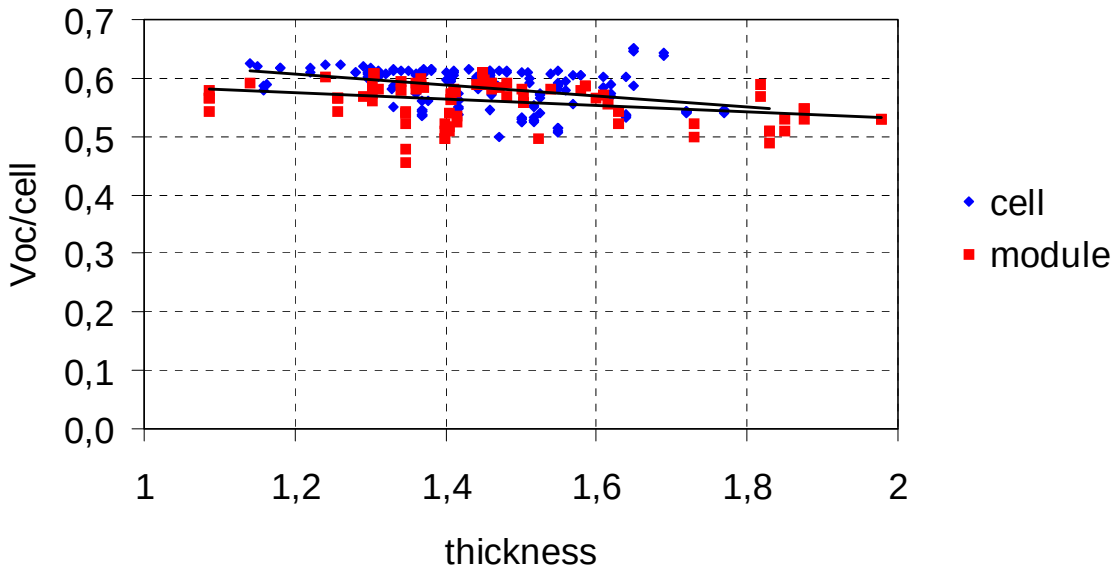

Fig. 20: Open circuit voltage of cells and submodules as a function of CIGS absorber thickness

Assuming that the thickness was the only varying property of the absorber layer, there is no straightforward explanation to the increased open circuit voltage with reduced thickness. In the same line of thoughts the observed short current loss at low thickness is lower than anticipated. In order to explain these observation additional properties of the CIGS absorber must be influenced by the thickness in the actual growth process. The following hypothesis is proposed.

The lower open circuit voltage at large thickness is related to lower Ga/(Ga+In) ratio in the top part of the CIGS layer. The Ga/(Ga+In) ratio depends on the intermixing of a Ga-rich bottom layer (the initial part of CIGS growth) and the top layer deposited at In-rich conditions. This intermixing is more enhanced at low thickness compared to the thicker films due to limited diffusion of Ga and/or In.

In order to check this hypothesis two processes (A and B) were compared. Process A has a pronounced difference in the Ga/(Ga+In) deposition ratio in the beginning and end of the growth, as described above, but in Process B the Ga/(Ga+In) ratio is much more constant throughout the CIGS growth. The efficiency data from devices fabricated from these two processes are presented in Fig. 21 and Fig. 22.

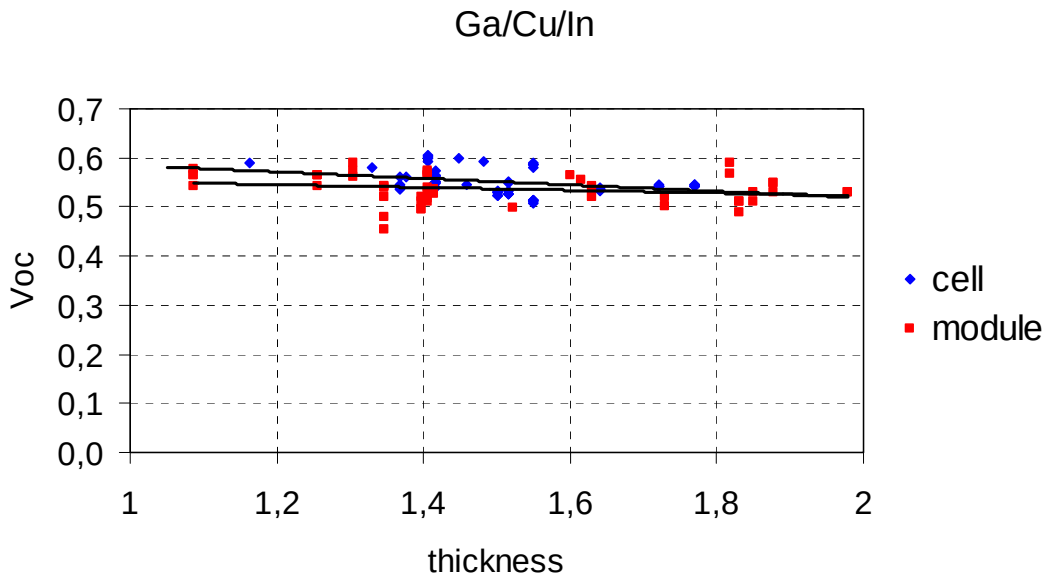

Fig. 21: Open circuit voltage of cells and submodules as a function of CIGS absorber thickness for CIGS films grown with a strong Ga/(Ga+In)-gradient

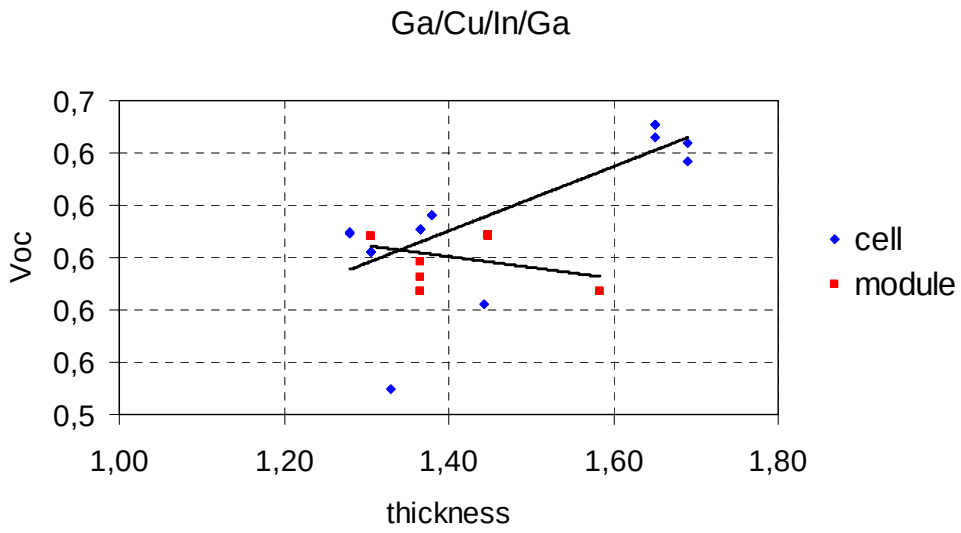

Fig. 22: Open circuit voltage of cells and submodules as a function of CIGS absorber thickness for CIGS films grown with a weak Ga/(Ga+In) -gradient

It is clearly seen by comparing Fig. 21 and Fig. 22 that the influence on efficiency from the thickness of the CIGS layer is much stronger with CIGS films grown under relatively constant Ga/(Ga+In) ratio. (Note there is only one data point relating to a submodule that falls out in Fig. 22. Such a variation is anticipated for relatively homogeneous CIGS layers whereas the weak dependency seen in Fig. 21 results from the counterbalancing effect of increasing the Ga gradient.

Absorber thickness further reduced – large modules (Solibro AB)

Reduced thickness of the CIGS layer has been tried both for full sized modules and for module stripes. In Fig. 23, the current density for modules and module stripes are plotted as a function of thickness. The spread is significant since it is a small series of modules, but it can be seen that the current density at 1.6 µm has not reached a stable value, which indicates that there are some loss in light absorption already at this thickness.

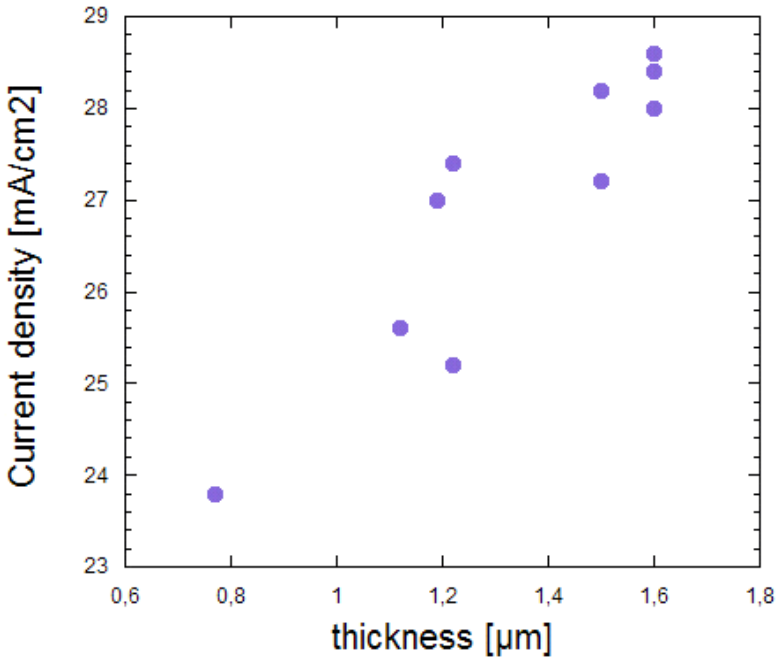

Fig. 23: Current density as a function of CIGS thickness for a series of modules with varying thickness prepared from the module line at Solibro.

The best "thin" modules are presented in Tab. 5.

Tab. 5: Solar cell module parameters for modules at different CIGS thicknesses. The modules at 1.6 and 0.75 µm CIGS thickness are full sized modules, whereas the module at 1.2 µm consists of a stripe with equal number of cells as the others, but with a width of 10 cm.

CIGS thickness	Voc/cell	Jsc	FF	eff
1.6 µm	600 mV	28.6 mA/cm^2	70 %	12 %
1.2 µm	605 mV	25.2 mA/cm^2	70.5 %	10.8 %
0.75 µm	577 mV	23.8 mA/cm^2	62.6 %	8.6 %

As can be seen, the current density decreases for the modules with decreasing CIGS thickness, but in the case with the thinnest CIGS layer also the voltage and fill factor are affected negatively.

Evaluation of reduced CIGS thickness and efficiency

A reduction of the absorber thickness below 1 µm does not seem to be favourable. It appears that there is a loss in short circuit current that is due to the dramatic reduction of the absorber thickness and that it cannot be compensated by improved back-contact reflectors or other measures taken to keep up the performance of the devices.

Solibro has performed a profit and loss calculation from an economical point of view. The calculation has shown that a reduction of the absorber thickness will only yield an economical advantage if the efficiency does not drop at all.

Thus it appears that a thickness reduction for the CIGS absorber has to be approached less aggressively. Therefore, a reduction of the absorber thickness down to only 1.4 µm was investigated in the next step.

Moderate thickness reduction and other parameters – large modules

The influence of reduced thickness on solar cell efficiency was studied for two cases of Cu content bins as measured by XRF.

Results are scattered, but the trend is that a low Cu-content (with a Cu/(In+Ga) ratio between 0.7 and 0.8) in general gives better results for very thin CIGS layers, whereas cells with more than 0.8 in Cu/(In+Ga) ratio suffers from mainly a decrease in fill factor.

The influence of reducing thickness down to 1.4 micrometers was investigated using the baseline Solibro process by making full size modules. A graph is presented in Fig. 24. The thickness reduction was obtained by reducing the evaporation rates and not the evaporation time.

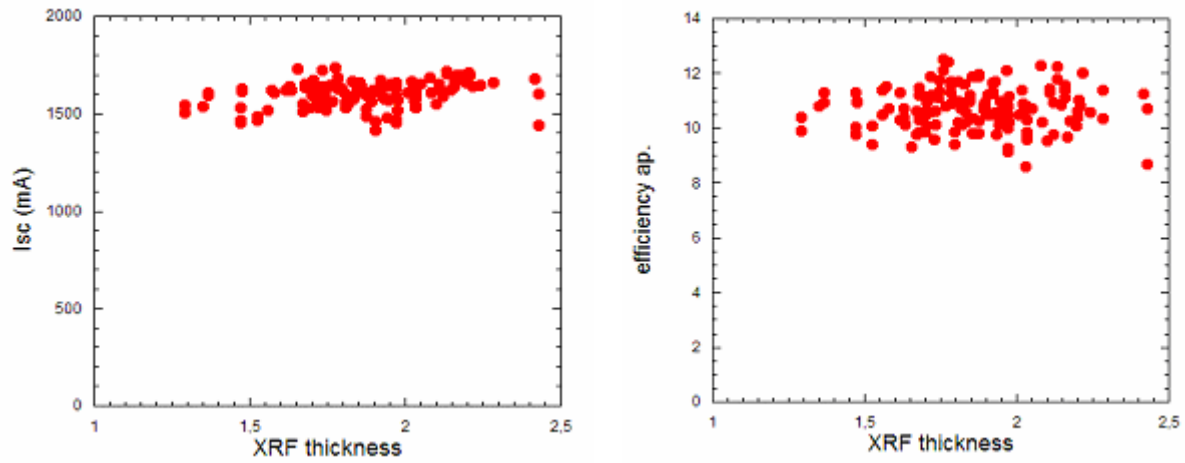

Fig. 24: Current density and efficiency as a function of thickness of the CIGS layer for a number of modules from prototype production.

The influence of the thickness reduction was observed in a reduced current density, but there was only a minor influence in the voltage and fill factor. In total, the efficiency was reduced by the thickness reduction.

Best full size module at 1.4 micrometer CIGS thickness had an aperture area efficiency of 11.3 %, corresponding to a 76 W module.

1.2.3.2 Graded CIGS process

Beside the activities on thin CIGS films we have also developed a graded CIGS coevaporation process. We have paid special attention to gradients in the gallium content x = [Ga]/[Ga+In].

The baseline graded CIGS process keeps the gallium content x at a constant level of about 27 % throughout the process.

Our findings make it clear that, for our process, gradients defined by variations of the evaporation profiles are to a good part retained even in the final films. This illustrates a pathway for engineering the bandgap in graded CIGS processes and consequently also indicates that one should be aware of incidental gradients in the profiles and avoid them if they alter the bandgap in a detrimental way.

Besides this, we observe a strong drop of the Cu content y in the topmost 200 nm of all investigated absorbers accompanied by a rise in the selenium content. These data correspond to the composition of the ordered-defect compound $Cu(In,Ga)_3Se_5$, which is believed to widen the bandgap by lowering the valence-band edge. Due to the gradual compositional transition and the absence of specific peaks in electron diffraction analyses, we think that this is a surface defect layer that does not form an individual phase.

As seen in Fig. 25, both back-side gradients and a *thin* front-side gradient improved the device efficiency, mainly by virtue of a higher open-circuit voltage. The higher Ga content at the back creates a back-surface field in the conduction band which prevents electrons from reaching the rear contact, thus reducing recombination there. The bandgap widening by the front-side gradient (possibly in addition to an effect of the surface-defect layer already present in the baseline), reduces the intrinsic carrier concentration at the *p-n* junction and thereby the interface recombination. (The higher current density in sample C, owed to a higher long-wavelength quantum efficiency, may be primarily an effect of a slightly thicker absorber.)

However, if a front-side gradient is too strong, it acts as a barrier for electrons on their way towards the junction. This causes voltage-dependent collection and at least the fill factor is severely reduced. In the extreme case, as for sample D in Fig. 25, the impact is even seen in the short-circuit current.

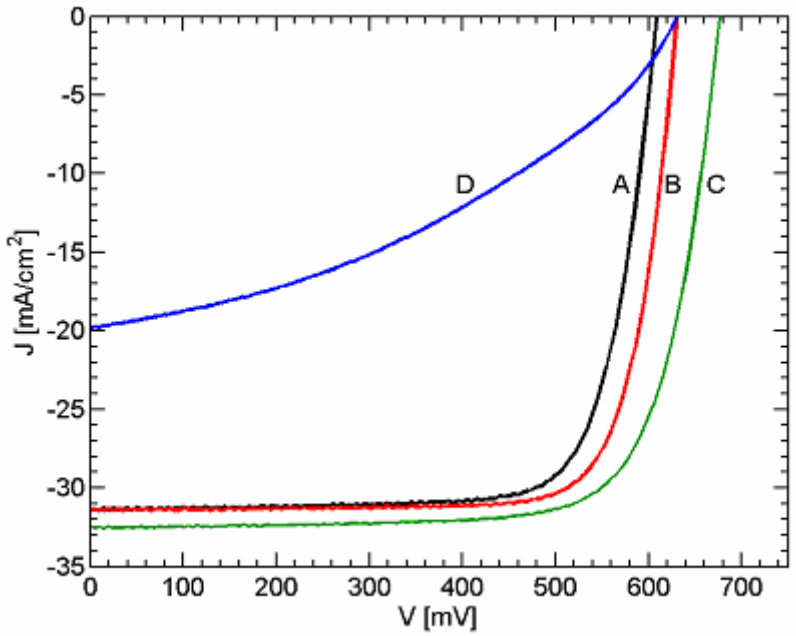

Fig. 25: Current-Voltage characteristics. A: Baseline without intentional gradients. B: Back-side gradient. C: Ditto, plus thin front-side gradient. D: Ditto but thicker front-side gradient.

Tab. 6: Current-Voltage results of the best cells (as deposited) of each sample

	J_{SC}	V_{OC}	*FF*	η
A	31.4	608	77	14.4
B	31.6	638	78	15.8
C	32.5	676	75	16.4
D	19.8	663	43	7.1

Tab. 6 lists the efficiencies of these cells which includes the maximum efficiency of 16.4 % without antireflective coating. Thus a new pathway for the production of CIGS solar cell devices has been established for highly efficient CIGS devices that serve the purpose of cost reduction in production.

Investigation of sodium incorporation methods into CIGS

CIGS solar cells for high efficiency devices require the incorporation of a small amount of Na into the absorber layer. For cells processed on soda lime glass substrates sodium can diffuse during CIGS deposition into the absorber.

We investigated the sodium supply via thermal evaporation from a NaF source during CIGS growth to develop a simple method, that allows controlling the incorporated amount of sodium, that is in-line compatible and that ensures high cell performance. In order to optimize the cell performance various aspects were examined:

- Variation of sodium amount
- Application of sodium during different stages of mulit-stage process

- Characterization of layer micro-structure and composition
- Variation of substrates materials (SLG, polyimide foil, stainless steel foil)

Here presented investigations were performed on evaporated CIGS layers grown on Mo coated soda-lime glass substrates that contain Si_3N_4 as intermediate diffusion barrier layer. CIGS layers of about 2 µm thicknesses were grown with three-stage co-evaporation process. The substrate temperature during CIGS deposition was kept below 450 °C.A controlled amount of Na was added in CIGS via co-evaporation from a NaF source.

Structural Na effects reported in literature are changes in CIGS grain size and texture, however, these effects seem to depend on the details of processing conditions, as contradictorily results are mentioned. We investigated the CIGS layer structure depending on time when sodium is added to CIGS. The structural effects of sodium incorporation during the different stages of the graded CIGS process are shown in SEM-micrographs of the CIGS cross-section (Fig. 26). Significant changes in the layer structure can be observed when sodium is evaporated during first growth stage (Fig. 26a) and during second growth stage (Fig. 26b), respectively. These layers show inhomogeneous grain size distribution containing a ≈500 nm thick region of small grains near the back contact and a ≈250 nm thick region at the top most region (cf. dashed line in Fig. 26a,b). Fig. 26c shows the CIGS-layer structure when sodium is incorporated during third stage of CIGS deposition. With this method a homogeneous layer structure can be achieved. Only the top most region reveals smaller CIGS-grains (cf. dashed line in figure), however this effect seems to be less distinctive compared to the structures shown in Fig. 26a and b. Fig. 26d presents a reference sample, which contains no sodium. The layer posses homogeneous distributed large grains up to a size of 1µm.

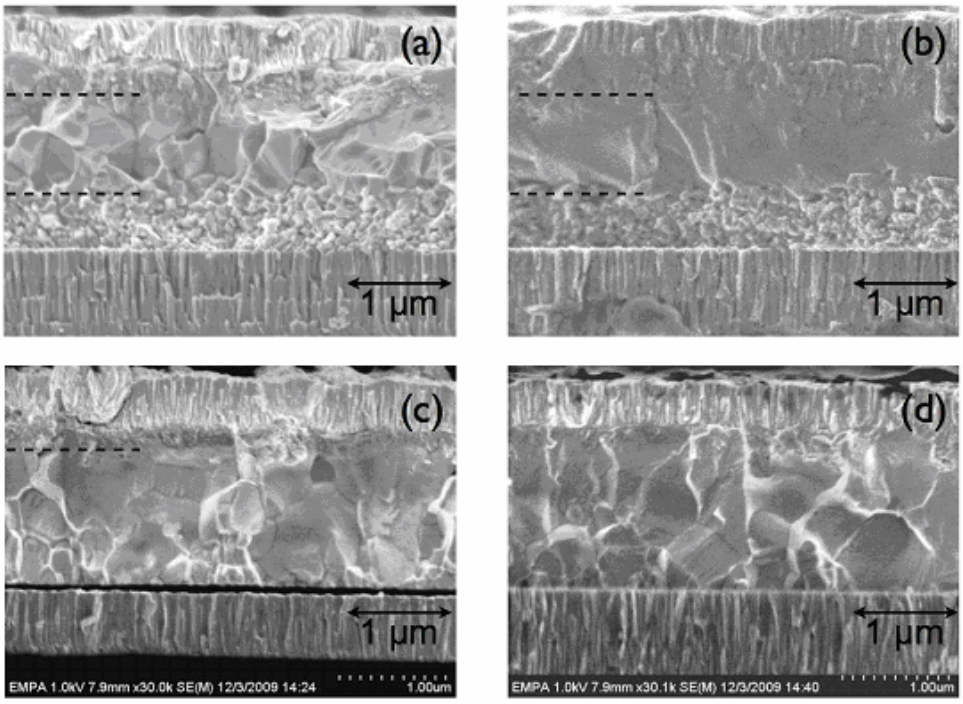

Fig. 26: SEM micrographs of CIGS layer cross section. Sodium was incorporated during CIGS growth via thermal evaporation from NaF source (a) in first CIGS growth stage, (b) in stage two and (c) in stage three. Picture (d) shows a reference sample without sodium supply.

In order to investigate the origin of inhomogeneous grain size distributions SIMS and Raman measurements have been performed by LARCIS project partners. Both measurements aim to analyze the distribution of elements across the layer.

Depth profile composition measurements – performed with SIMS, presented in Fig. 27, revealed that CIGS absorber layers have a complex graded composition across the layer thickness. All layer exhibit an intermediate Ga poor region and a Ga rich back region. However, it can be seen that the grading and variation of Ga is more pronounced when sodium is added during the the first and second stage of CIGS growth process. The presence of regions with different Ga content has a strong impact on the microstructure of the samples. In particular at high x-values (x=Ga/(In+Ga) the formation of small grains is reported in literature. Thus SIMS measurements are in agreement with the observations from SEM-micrographs.

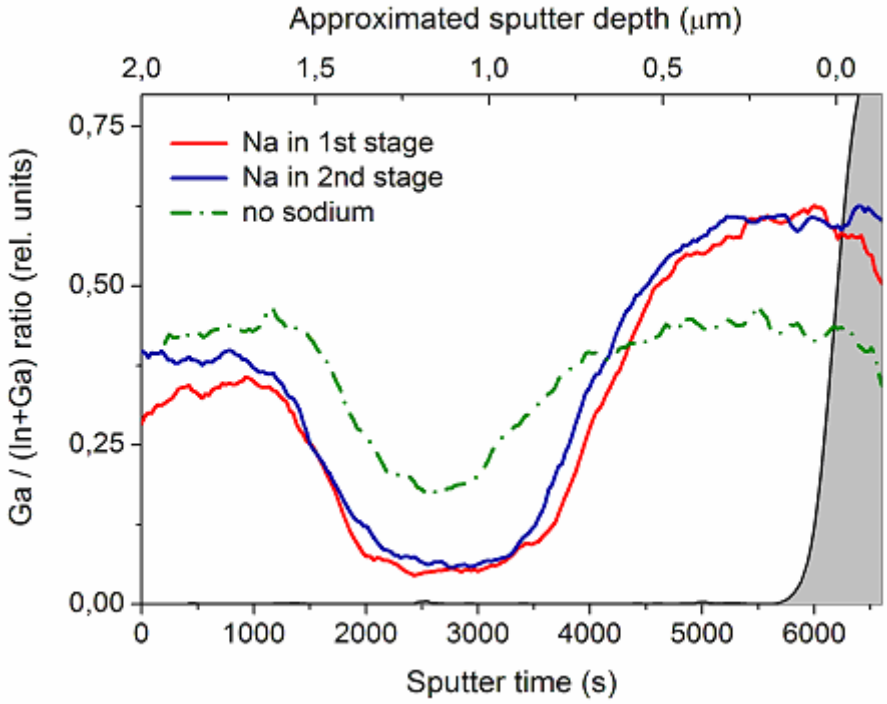

Fig. 27: Relative Ga/(In+Ga) concentration as obtained by SIMS measurements. Data for sodium application during 3rd stage are still under way.

Features, as structural and compositional inhomogeneities, complex grading profiles of elements and chemical phases in CIGS layers has been analyzed for the first time with Raman technique. For CIGS alloys, the frequency of the main A_1 Raman mode shows a linear dependence on the Ga content. It increases linearly with the Ga content from the position corresponding to stoichiometric $CuInSe_2$ (reported at 173 cm^{-1} at 300K) to that of stoichiometric $CuGaSe_2$ (reported at 184 cm^{-1} at 300 K). In combination with an optical microscope for both excitation and light collection (Raman microprobe), a high spatial resolution (below 1 μm) can be achieved. This opens the possibility for the direct inspection of the cross-section of thin CIGS layers, providing information on the presence of regions with different Ga content.

Fig. 28 shows the Raman spectra measured with the laser spot focused at different positions on the cross-section of the layer, together with that directly measured at the layer surface.

The lateral region contributing to spectra of the cross-section is determined by the diameter of the laser spot of about 0.7 mm. For a compositionally inhomogeneous layer this implies that adjacent regions of different composition (e.g. Ga/In ratio) in the layer might contribute to the spectrum measured with the laser spot at a given position. In contrast the spectra obtained directly from the layer surface contain depth information in the order of only 100 nm, being this determined by the strong absorption of light in the CIGS alloy.

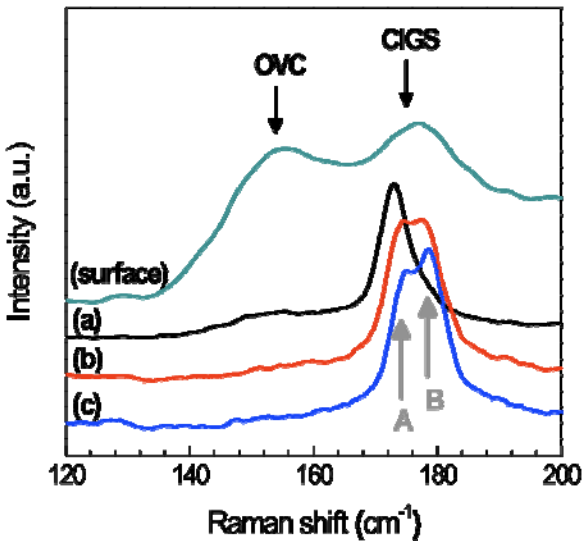

Fig. 28: Micro-Raman spectra measured at the surface of the CIGS layer and with the laser spot focused at different positions of the cross-section of the CIGS layer: (a) surface region, (b) mid region, (c) back region. The spectra are normalized to the intensity of the main A_1 CIGS mode, and the spectra measured at different regions from the layer are vertically shifted.

The spectrum from the surface of the layer is characterized by the presence of a broad contribution at a lower frequency of about 155 cm^{-1}, in addition to the main A_1 peak from the CIGS phase at about 178 cm^{-1}. The contribution at 155 cm^{-1} has been identified as the main vibrational mode characteristic for a Cu-poor OVC phase. The presence of this mode in the spectrum suggests a Cu-poor surface composition in the CIGS layer. On the other hand, the A_1 CIGS mode is shifted towards higher frequencies in relation to that from $CuInSe_2$ (173 cm^{-1}). This indicates the presence of a significant Ga content at the surface region.

The spectrum measured at the top surface contrasts with the spectra measured from the cross-section of the layers, where no OVC spectral contribution is detected. The cross-section spectra show two distinct contributions, that can be resolved by fitting with Lorentzian curves, with peaks at about 173-174 cm^{-1} and 178-179 cm^{-1}, respectively (labeled as A and B contributions in Fig. 28). The analysis of measured peaks confirms inhomogeneous composition grading: spectrum marked (a) in Fig. 28 indicates the existence of a sub-surface region, with very low Ga content. A back region with a much higher Ga content in the order of 55% is indicated by spectrum marked (c).

Further Raman measurements with higher in-depth resolution were performed for refinements and cross validation by acquiring sequentially a series of Raman spectra after sputtering the sample with the Ar^+ beam. Estimated penetration depth of scattered light is about 100 nm.

Fig. 29 shows the sequence of spectra measured at different depths after sputtering the layer surface. These spectra corroborate the existence of an OVC phase at the surface region. Spectra (curves a and b) recorded with sputter times less than 10 min (corresponding to a layer depth less than about 470 nm) show again a significant frequency contribution at 155 cm^{-1}. The inset in Fig. 29 shows the dependence of the frequency of the A_1 mode on the sputter time. As already suggested by the cross-section measurements, a minimum frequency value of about 173 cm^{-1} – corresponding to a region with very low Ga content- is observed at the intermediate region, and the maximum frequency of about 179 cm^{-1} – corresponding to a region with high Ga content- is observed at the region close to the back interface with the Mo coated substrate.

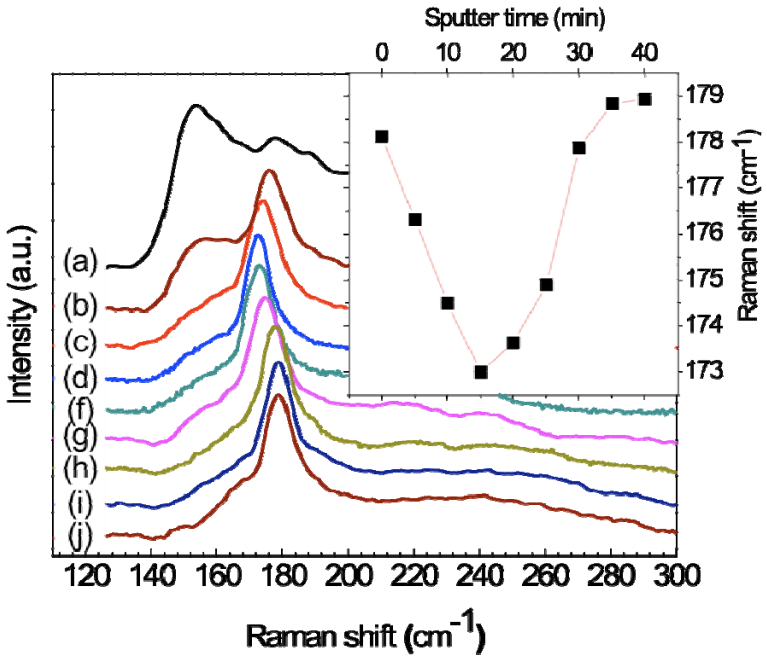

Fig. 29: Raman spectra measured after sputtering CIGS layer with different times: (a) 0 min, (b) 5 min, (c) 10 min, (d) 15 min, (e) 20 min, (f) 25 min, (g) 30 min, (h) 35 min, (i) 40 min. The spectra are normalised to the intensity of the main A_1 CIGS mode, and spectra obtained after different sputter times are vertically shifted. Inset in the figure shows the plot of the frequency of the A_1 CIGS mode versus sputter time.

The work on sodium incorporation methods revealed various effects related to absorber microstructure, element distribution as well as related to electronic properties of CIGS layer. The origin of inhomogeneous microstructure as observed in SEM micrograph was identified with SIMS and Raman measurements. Results from both methods have concordantly shown, that a significant variation in Ga concentration across the layer thickness causes these inhomogeneities in CIGS grain sizes, rather than the presence of sodium. On the other hand, the strong Ga grading can only be observed when sodium is present during the CIGS growth. This implies, that the presence of sodium impedes the inter-diffusion of elements and finally preserves the grading introduced by the growth process.

The electronic properties of CIGS are strongly influenced by the Ga-grading within the absorber layer. The optimization of this Ga grading can lead to further improvements of cell performance and hence, insights gained from the above experiments might become important for controlled tailoring of composition grading.

However, the mechanisms in which sodium could increase electronic properties of CIGS are still not completely understood. Further investigation will aim to localize the incorporated sodium within the CIGS, to analyze whether it acts within the CIGS grains or at the grain boundaries and to gain insights of how sodium influences the diffusion of elements.

Modification of the graded CIGS growth process

We have modified the graded growth process by reducing the deposition time during the first growth stage and by extending the duration of the second and third stage. The material consumption for this process remains the same as for standard process but the layer formation is now influenced/modified by a longer duration at which the composition of growing CIGS-absorber is in Cu-rich state. The duration under Cu-rich condition to what the second stage extends the first stage defines the Cu-excess.

Fig. 30(a) shows the average cell efficiencies obtained from experiments with changed Cu-excess. The efficiency increases with the extension of the second stage until an optimum value is reached at 25% Cu-excess.

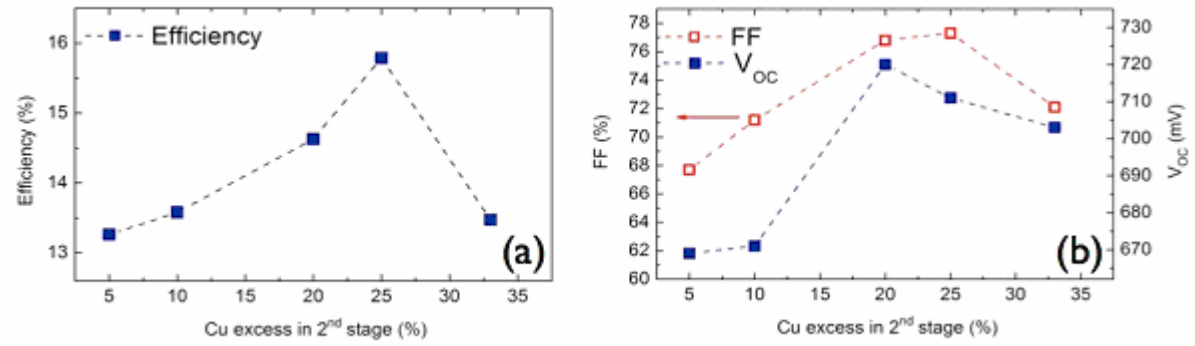

Fig. 30: (a) Efficiency, (b) Fill factor (FF) and open circuit voltage (V_{OC}) as function of Cu-excess. An optimum in device efficiency can be obtained when the duration of second stage extends the duration of first stage by approx. 25%.

This result again shows the high potential of the graded CIGS growth process with regards to high device efficiency and also cost efficiency. For industrial application, however, it appears to be very important to fine-tune the exact processing parameters in order to exploit the full potential of this promising manufacturing technique.

Transfer of the graded CIGS processing to the pre-production level

It appears that a good method to reduce production cost could be the implementation of this graded CIGS high efficiency lab processes into the production environment. An increase in device efficiency could improve the cost-per-Watt-peak ratio.

The graded absorber process has shown this potential in the lab environment and therefore has been implemented and investigated in an inline deposition system at the ZSW. A long-term

comparison of small area cells produced with this system as depicted in Fig. 31 shows that the graded CIGS process has a much higher efficiency potential than the formerly used single-stage process. The increase of the average long-term efficiency is 2.2 %. This is a very significant increase that clearly justifies a transition from a single-stage to a graded process in a production environment despite the fact that the latter is more complex.

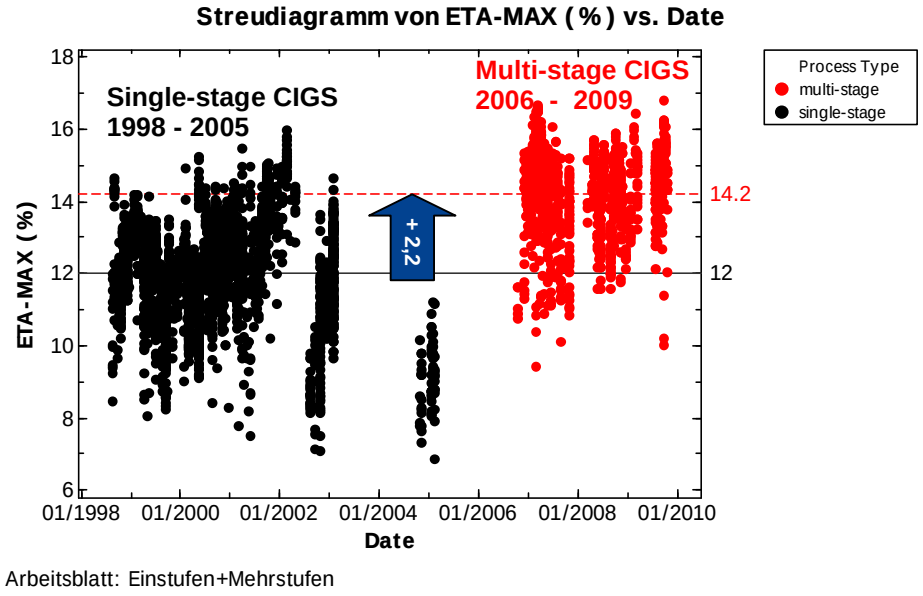

Fig. 31: Long-term comparison of inline single-stage and graded CIGS process by the comparison of the maximum efficiency of small area cells of each carrier processed from 1998 to 2005 and 2006 to 2009. The graph is corrected in the last part where a different grid design was used. The difference between the two process types is 2.2 % in efficiency which shows a clear superiority of the graded CIGS process.

By the variation of the Selenium rates and the application of interface treatment procedures a remarkable maximum efficiency of 19.6 % (0.5 cm^2 / with anti reflective coating / certified by Fraunhofer ISE). Fig. 32 shows the IV-curve of this cell. This is particularly remarkable as this result is a new European record and this record has been produced on pre-production equipment and not on small lab machines.

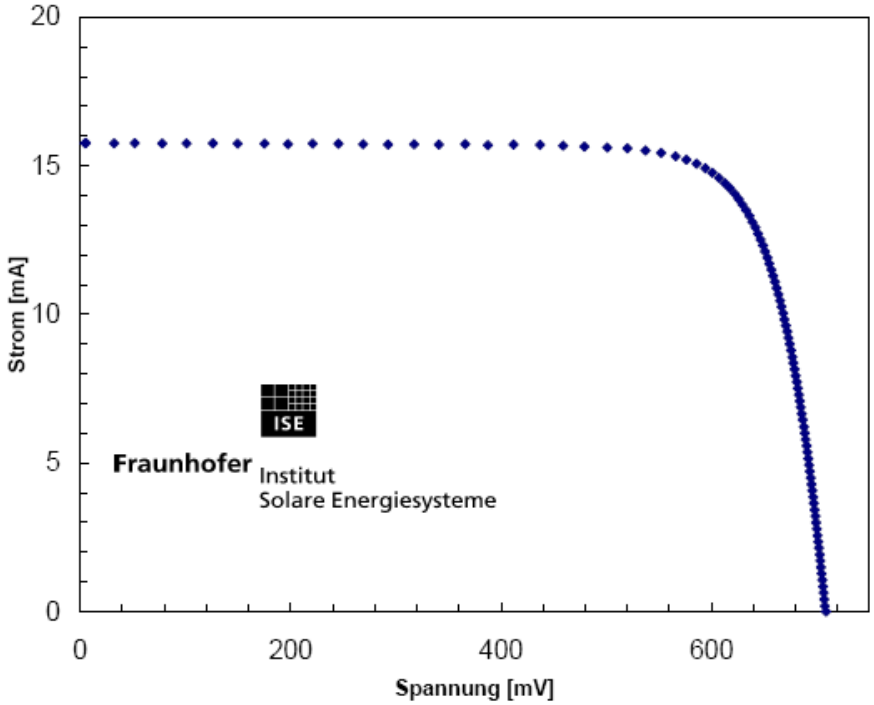

Fig. 32: IV-curve of 19.6 % cell produced on a pre-production system at the ZSW with the graded CIGS process.

The efficiencies obtained on the same production line of 30 x 30 cm^2 module have also been improved. The best module efficiency is 14.1 %, which is an increase of about +11.0 % relative compared to the best module efficiencies reached with the single-stage process (Tab. 7).

Tab. 7: Comparison of the maximum and average efficiencies of the inline single-stage and graded CIGS process. A relative gain of approximately 20 % in CIGS quality could be reached. For modules this gain is 11.0 %.

	Inline single-stage 1998 – 2006	Inline graded 2006 – 2009	relative
Maximum cell efficiency (0.5cm^2, w/ ARC)	16.1 % *	19.6 % *	+ 21.7 %
Average cell efficiency (0.5cm^2 w/o ARC)	12.0 %	14.2 %	+ 18.3 %
Maximum module efficiency (30×30cm^2)	12.7 %	14.1 %	+ 11.0 %

*) independently certified by Fraunhofer ISE

Further adaption of the non-CIGS related process steps should lead to even higher module efficiencies that correspond to the CIGS quality gain in small area cells obtained by the introduction of the graded CIGS process.

Evaluation of cost reduction approaches

One of the main tasks of the project was the evaluation of the investigated cost reduction methods.

Three main approaches have been chosen: cost reduction by …

1. buffer free cells
2. reduction of CIGS thickness
3. implementation of graded CIGS process into inline deposition system

The omission of a complete process step as suggested in the first approach "buffer free cells" sounds promising and would certainly lead to a cost reduction if the necessary equipment, floor space, and consumables for a whole process step could be avoided. However, the work on this approach within the project yielded only low efficiencies.

Consequently, it must be concluded that approach number one is still in an immature state. Perhaps "buffer free cells" will once more be under investigations if the physical and chemical requirements for the pn-junction interface are better understood.

For approach number two, the "reduction of CIGS thickness", has enjoyed most of the attention in the project as it produced promisingly high efficiencies of 17.7 % at 1.4 µm CIGS thickness whilst saving about 35 % of the CIGS material costs.

However, CIGS cells with thin CIGS layers tend to loose light from the red end of the solar spectrum by recombination of charge carriers that are generated at the back-contact by long wavelength photons. To remedy this situation a ZrN reflector was placed at the back-contact in order to reflect long wavelength photons so as to increase the probability of absorption in the volume of the CIGS layer near the pn-junction.

The investigation showed that the use of a ZrN back reflector was not as straight forward a solution for the saving of the long wavelength photons as expected. Seemingly, the replacement of the interface partner towards the back-contact of the CIGS solar cell by ZrN changed not only the reflective properties of the back-contact but also the electrical. These electrical effects, however, are negative, so that the efficiencies remain significantly reduced compared to standard cells with standard CIGS thickness.

The third approach to the reduction of production cost is the implementation of the most successful CISG process that has been used in lab environments up to now into an inline pre-production evaporation system. This work has been done by adding another vacuum chamber to an existing CIGS evaporation system.

The efficiencies of the devices produced with this new process showed a much higher efficiency than with the traditional simpler CIGS process shortly after the introduction of the new inline graded CIGS process.

The optimisation of this new CIGS process has lead to an increase in the long-term average efficiency of 2.2 % (absolute). The maximum efficiency obtained on this pre-production system is 19.6 % (small area cell), a new European record. It is most remarkable that hardly any loss in efficiency could be observed by the move from a lab machine to a pre-production inline deposition system.

In order to properly evaluate the potential of the most promising cost reduction methods investigated in the project – thin CIGS and graded CIGS processing – a detailed cost calculation has been performed on the basis of real numbers coming from the two industrial partners of the project.

This calculation accounts for the fact that one the original goals was to reduce the CIGS thickness and CIGS material costs by 25 % or 50 % and that this would result in a profit of 5 % and 10 % respectively. The experimental reality, however, shows that despite all efforts,

promising results, and significant material cost savings, the cell and module efficiencies cannot be maintained on the original level after having reduced the CIGS thickness significantly.

In addition, the cost of the CIGS material is only indirectly correlated with the profit of the end product. But the device efficiency affects the profit directly. Consequently, even a high percentage of material cost savings combined with only a very small loss in efficiency in the end yields a loss in profit.

At the same time the combination of unaltered high material costs and significantly increased efficiencies by the introduction of the inline graded CIGS process and all necessary optimisation measures yield a very significant benefit for the profit.

Thus, the comparative cost calculation clearly shows that any cost reduction methods that are supposed to save money in the production of CIGS modules can only do this if they do not affect the high efficiency level that standard devices can obtain.

Quite in contrast to common industrial thinking it appears to be worth while to even implement more costly procedures if only by them the device efficiencies can be increased as it is the case with the new inline graded process.

Thus, the overall result of the project´s investigations concerning cost reduction is that the introduction of production procedures like the graded CIGS process that have the capability to increase the device efficiencies is the central key to cost efficiency in the industrial production of CIGS modules.

As logical result both industrial partners of the project have now been responsive to these results by testing the inline graded CIGS process in production.

Thus we should expect a further significant increase of large area CIGS module performance in the European industry very soon.

Transfer of graded CIGS processing to the production level at Solibro GmbH

Presently, the champion module efficiency at Solibro GmbH production is at 13.5 % aperture area efficiency. In order to advance the technology and look ahead at higher efficiency, Solibro during this project period has started to investigate a graded CIGS co-evaporation process. The best result obtained from the first experiments was a small area cell with an efficiency of 16.9 % (no AR).

Transfer of graded CIGS processing to the production level at Würth Solar

WS has commissioned a new 60 cm x 120 cm CIGS deposition system that is capable of running an inline graded process. Several test runs have been performed in the final project period. Average and maximum module efficiencies are still slightly lower compared to the standard CIGS process.

Due to differences in the inline deposition systems between ZSW and WS, the recipe developed at ZSW could not be transferred to WS without changes. This is probably one of the main reasons why the efficiency improvement observed at ZSW could not be achieved at WS yet. Other reasons for the lower module efficiency compared to the standard process are inhomogenities of the CIGS deposition as well as adhesion problems between the Mo back contact and the CIGS layer. A variation of molybdenum sputter parameters will be necessary to develop a back contact suitable for inline graded CIGS. In addition, all the other processes

before and after CIGS deposition are also optimised for the standard CIGS process and may have to be modified for inline graded CIGS.

Process control of the inline graded process is much more complex than for the standard process. The resulting lack of reproducibility is the main reason for the spread of results and lower process yield compared to the standard process. It is expected that this could improve with experience with the new process in the near future. Moreover, additional process control methods. The application of such methods could also help to improve reproducibility.

It could be shown in the project that the inline graded process on large area is working in principle in the production environment of WS. Process development at WS is still in the starting phase, but the ZSW results for inline graded deposition show the promising potential of this method. WS therefore intends to continue developing and optimising this process.

1.2.4 Electrodeposited absorbers

Introduction: The situation of IRDEP has been modified during the last year of the LARCIS project. NEXCIS has started in July 2009 and the staff in charge of the work package "Electrodeposited Absorber" has changed. It is necessary to explain briefly IRDEP evolution to understand the next part of the document.

From 2005 to 2008, IRDEP (joint "Institute of Research and Development on Photovoltaic Energy" of ENSCP, CNRS and EDF) developed intensive researches on electrodeposited $CuInSe_2$ processing followed through sulfurization by rapid thermal process. The development of the $CuInS_2$ technology has allowed the creation of NEXCIS which will improve the performance of CIS cell on a large scale. IRDEP enhances its activities of Ga insertion by modifying its procedures.

1.2.4.1 Objectives and starting point of work

At the laboratory scale of small area cells, the record efficiency is 11.4% and 6.8% on 30 x 30 cm^2. The aims of this work package were:

- to increase these numbers to at least $\eta = 14\%$ and $\eta = 10\%$ respectively
- to demonstrate and improve the electrodeposition process on 30 x 30 cm^2 in terms of reproducibility, robustness of the process and yield.

These cells will be fully processed as modules according to the standard technology of the CISEL process. When available, the results from the Cd free buffer will be transferred to the electrodeposited modules in replacement of the CdS. To improve reproducibility and controllability of the process, inline quality assessment and quality control will be developed using Raman scattering.

1.2.4.2 Progress towards objectives – tasks worked on and achievements made

Two tasks composed this work package, the first one was about the enhancement of cell efficiency, the second about the scalability of the electrodeposition step. For the last period of the project, the results concerning the enhancement of cell efficiency (task 1) have been obtained at IRDEP. The results concerning the large scale development (task 2) have been transferred to NEXCIS who will further develop this technology.

Enhancement of cell efficiency

IRDEP enhances its activities on Ga insertion by using new procedures. In the next part we present firsts results on the control of composition of the absorber and the evolution of cell performance. We end that paragraph with an overview on IRDEP work.

Control of the composition of the absorber

The aim of composition of the absorber is a ratio of Ga/(Ga+In) = 30%. The new procedure in place allows to control and reproduce that composition. The composition characterizations are carried out by X-Ray Diffraction and X-Ray Fluorescence. The Fig. 33-(i) is an X-Ray diffractogram on a sample annealed under Se atmosphere. Inset shows the (112) reflection on an extended scale and its fitting with 3 Gaussian curves, corresponding to average composition of $CuIn_{0.65}Ga_{0.35}Se_2$. We see quantitative Ga insertion in the chalcopyrite in correlation with X-Ray fluorescence (Fig. 33-ii) : the measured composition corresponds to the one deduced using deconvolution of RX spectra.

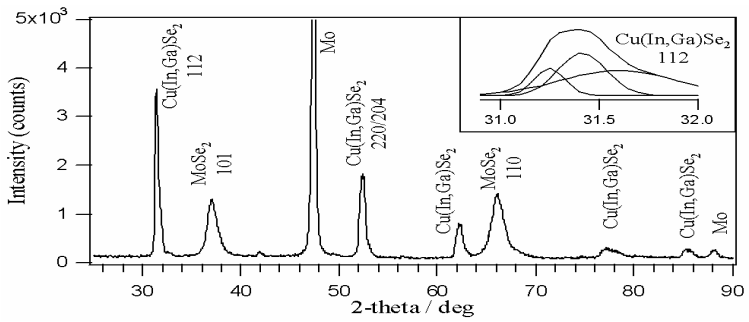

(i)

% Cu	14,9 %
% In	9,7 %
% Ga	4,7 %
% Se	70,8 %
Ga/(In+Ga)	33 %

(ii)

Fig. 33: ***(i)*** *XRD pattern of a selenized sample.* ***(ii)*** *Composition measured by X-ray fluorescence. Inset in the left figure is a zoom on the (112) peak of $Cu(In,Ga)Se_2$ chalcopyrite.*

Electrical characterisation

Now we propose to examine the electrical performance of such an absorber covered by a CdS layer (chemical bath deposition) and a sputtered ZnO-i and ZnO-Al layer.

Fig. 34-(i) is an I-V measurement of an 0.1 cm^2 absorber with the composition presented in the table on the right (

Fig. 34-ii). The optoelectronic results are summarised in the table at the bottom of the two last figures (see

Fig. 34-iii).

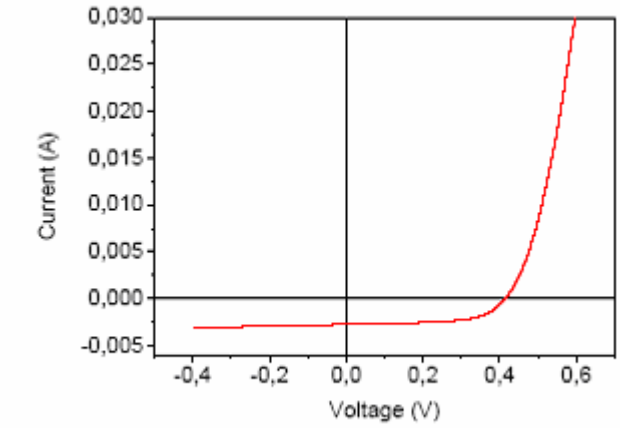

(i)

% Cu	18 %
% In	16 %
% Ga	7 %
% Se	59 %
Ga/(In+Ga)	30 %

(ii)

1.1 Eff	1.2 Voc	1.3 Jsc	1.4 FF	1.5 Rsh	1.6 Rs
7,06%	1.6.1 416V	28 mA.cm^{-2}	61%	1189 Ohms	19,8 Ohms

(iii)

*Fig. 34: **(i)** I-V characterization on 0.1 cm^2. **(ii)** Composition measured by X-Ray fluorescence of the absorber Cu(In,Ga)Se$_2$ of the cell characterised. **(iii)** Electrical performances of the measured cell.*

At IRDEP we have obtained CIGS solar cells with 7 % efficiency, an open circuit voltage of 416 mV and short circuit current density of 28 mA.cm^{-2}. In the next paragraph, we will show the evolution of our best cell.

Reproducibility and evolution of the performance

In this paragraph we present results on several cells of 0.1 cm^2. First we show that for all these cells the ratio of Ga is controlled and is nearly equal to 30 % (Fig. 35-i). For each cell, the increase of efficiency is significant and the best cell obtained has 8% efficiency (Fig. 35-ii). Concerning the open circuit voltage (blue triangle in Fig. 35-ii), the improvement does not follow a linear evolution like the efficiency but seems to reach a step at 420 mV except for the best cell which present 375mV. The current density (black square in Fig. 35-iii) has an evolution of up to 35 mA.cm^{-2} like the fill factor up to 60% (blue triangle in Fig. 35- iii).

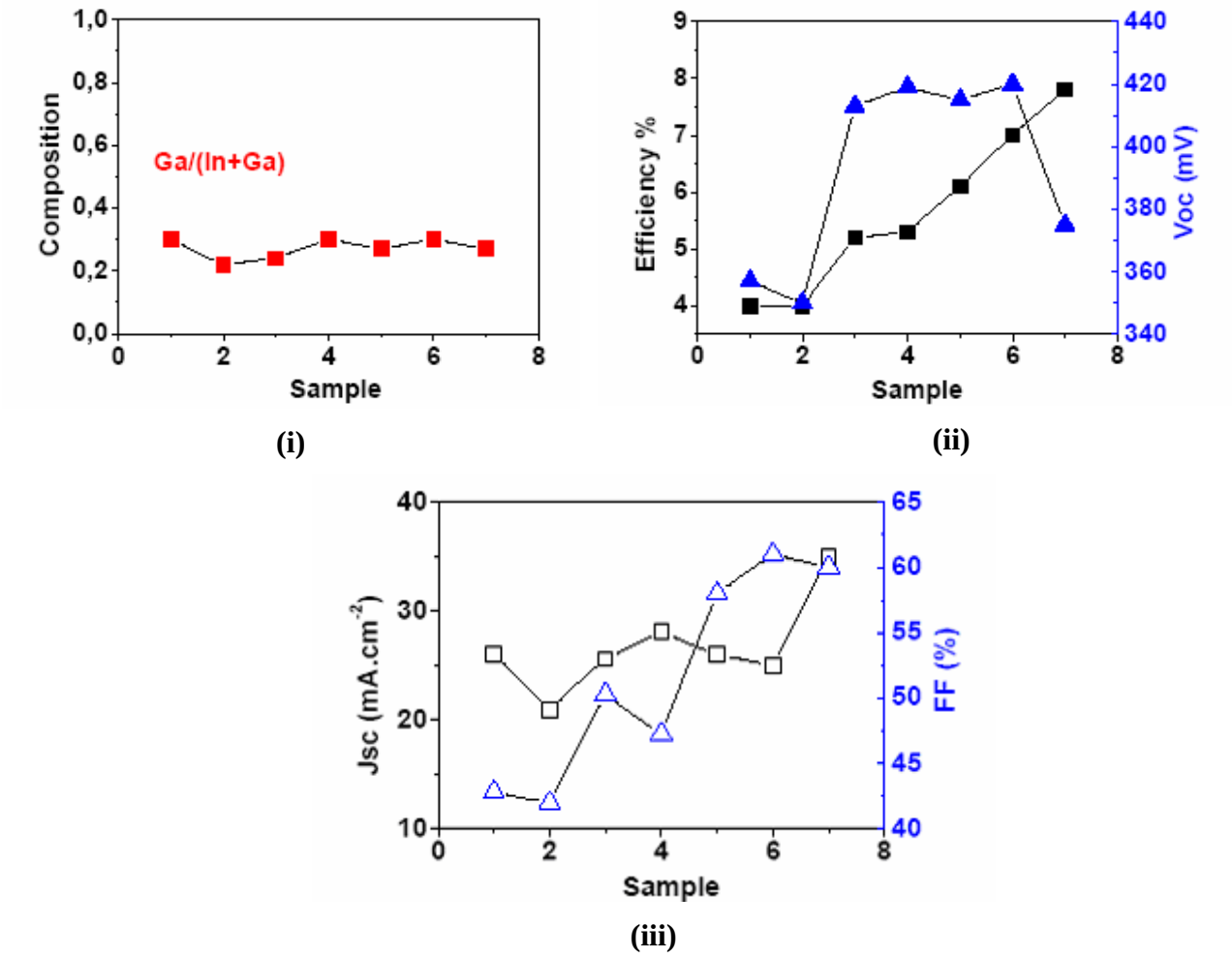

Fig. 35: ***(i)*** *Evolution of the Ga/(Ga+In) ratio as a function of the samples.* ***(ii)*** *Evolution of the efficiency (black square) and Voc (blue triangle) as a function of the samples.* ***(iii)*** *Evolution of the Jsc (black square) and FF (blue triangle) as a function of the samples.*

Overview

The new procedure of Ga insertion has proven its efficiency in terms of composition control and performance. 7.8% efficiency have been reached for the best cell. IRDEP goes on improving it by stabilizing the electrodeposition procedure and working on the reproducibility on small area (<1cm^2). New kinds of annealing processes have to be tested and analysed in order to understand the mechanism of recrystallisation.

After this step, cells of 5 x 5 cm^2 will be tested.

Scalability of the electrodeposition step

As announced at the beginning of this chapter, the results produced about the scalability of the electrodeposition step are provided by Nexcis. Nexcis develops its process on large scale using two approaches concerning the electrodeposition: the one-step process and the stack process. The first one is a coelectrodeposition of copper, indium and selenium on molybdenum from a single bath followed by a sulfurization with rapid thermal process. The second one is a succession of depositions of copper and indium on molybdenum and then incorporation of sulphur by thermal treatment. In the next part, the problems and work in

progress relative to each approach are presented. Then the results on 5 x 5 cm^2 and 15 x 15 cm^2 are shown. An overview of Nexcis work is proposed.

One step process

The one step process is complex to manage since the bath stability is complicated to control (see paragraph 1.2.4.3) and since there is a strong impact of the mass transfer on material properties. Nevertheless, the process could be well controlled up to 30 x 30 cm^2. Main challenge is the presence of the back diode layer $CuIn_5S_8$ after thermal treatment. The origin of the formation of the spinel type $CuIn_5S_8$ after annealing is the electrodeposited binary phase Cu_xSe.

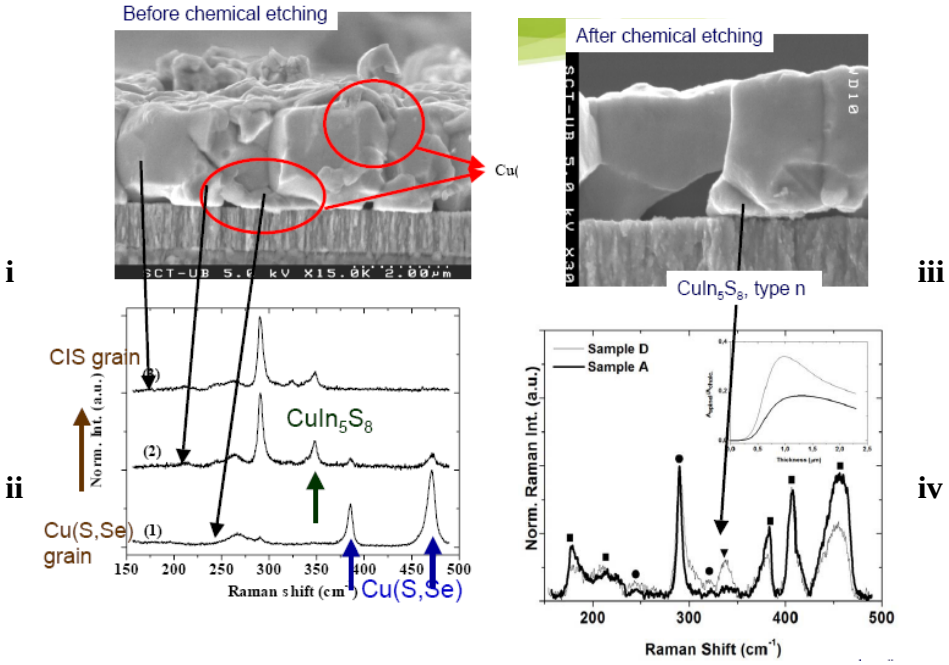

Fig. 36: ***(i)*** *Cross section of an absorber before chemical etching observed by MEB-FEG.* ***(ii)*** *Raman spectrum corresponding to the last cross section.* ***(iii)*** *Cross section of an absorber after chemical etching.* ***(iv)*** *Raman spectrum corresponding to this cross section*

Fig. 36-(i) is a cross section of an absorber before chemical etching. The phases along the cross section are identified on a Raman spectrum (Fig. 36-ii). We see that the large grains are composed of $CuInS_2$. If we look near the molybdenum surface, the spinel phase appears. At the boundaries of the grains the binary phases are circled on the Fig. 36-i. After chemical etching, the binary phases disappear (Fig. 36-iii) and the spinel phase is still put in evidence (Fig. 36-iv).

The works in progress concern the indium incorporation by electrodeposition during the first step of $CuInSe_2$ growth. The second aspect is an improvement of the annealing conditions.

Stack approach

The second approach used by NEXCIS is the stack Cu/In deposition. The main problems are the substrate preparation before electrodeposition, the enhancement of Cu-In interdiffusion

(formation of the $Cu_{11}In_9$) and to avoid the formation of Cu_xS near the back contact. The problem of adhesion of the absorber on molybdenum is shown in Fig. 37.

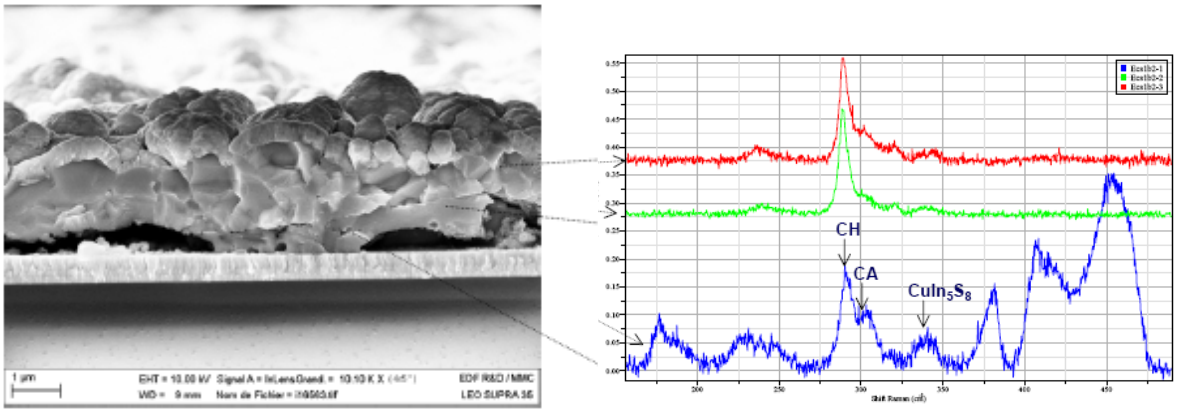

(i) **(ii)**

Fig. 37: ***(i)*** *Cross section of an absorber observed by MEB-FEG. (ii) Raman spectrum corresponding to the cell observed on cross section*

Fig. 37-i shows that the absorbers synthesised by stack approach do not adhere on the molybdenum. The phases along the cross section are identified and we observe that near the back contact the Cu-Au and the spinel phases are present. The suppression of these phases is the main issue for this electrodeposition approach.

Results

The first results using stack approach followed by annealing in sulphur atmosphere are obtained on a 5x5 cm^2 cell. The Fig. 38 is a cell engraved with 0.1 cm^2 pixel, the average efficiency is 7.7% and the maximum efficiency is 8.8%. The efficiencies for each cell are written. In the center of the cell the performances are better than at the edge where the efficiency can be 3.3 %.

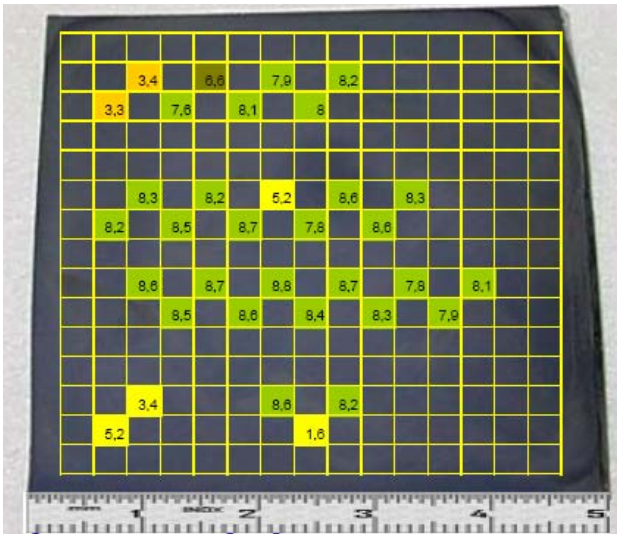

Fig. 38: Distribution of efficiencies on a 5x5 cm^2 cell synthesised with stack approach.

The process scale-up from 5 x 5 cm² to 15 x 15 cm² has started at Nexcis in August 2009. On larger surface (15x15 cm^2 cells) the edge effects are still identified but are improved compared to those observed on 5x5 cm². Despite edge effects, the average efficiency is 8.14% and the maximum is 8.81%. The Fig. 39-i represents a 15x15 cm^2 cell engraved in the center forming a cross . Except the 3 cells at the top, the distribution of efficiency is quite homogeneous. If we look more precisely (see Fig. 39-ii) , the efficiencies of the cells are better in the center than at the edge. The yellow cells in Fig. 39-ii have an efficiency less than 5%.

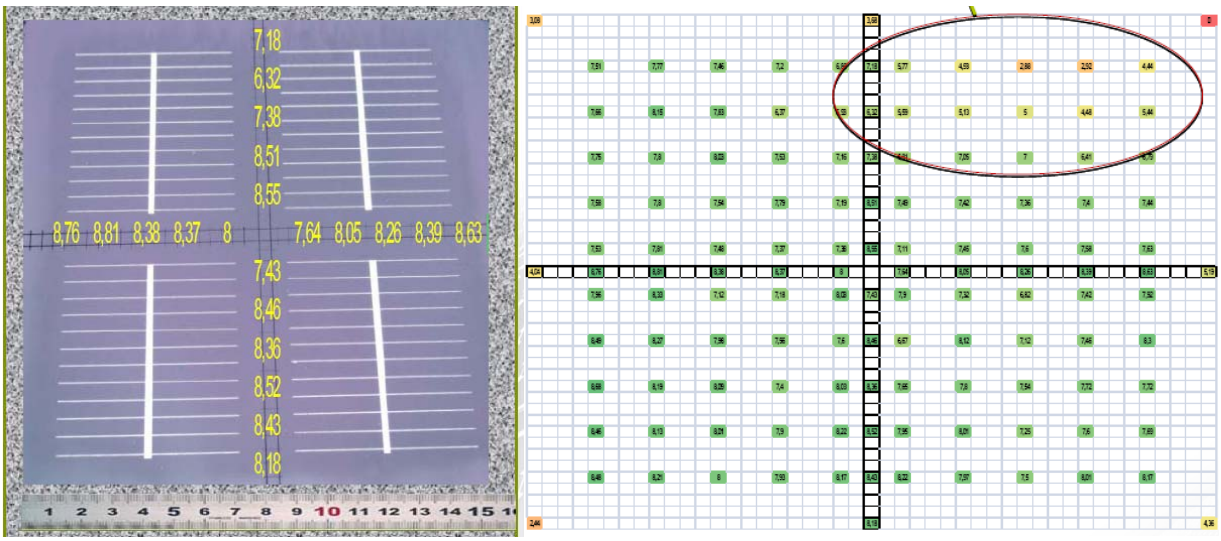

(i) **(ii)**

Fig. 39: ***(i)*** *Distribution of efficiencies along a cross on a 15x15 cm^2 cell synthesised with stack approach. (ii) Distribution of efficiencies on all the 15x15 cm^2 cell.*

A particular attention has been paid on the difference of efficiency on 15x15 cm^2 samples. On the edge, adhesion between absorber and molybdenum is bad, the recristallisation is not complete (Fig. 40-i) and there are binary compounds at back contact (see Fig. 40-ii). On the other hand, in the centre of cells where the efficiencies are better, the adhesion is good (see Fig. 40-iii) and we cannot observe secondary phases (see Fig. 40-iv).

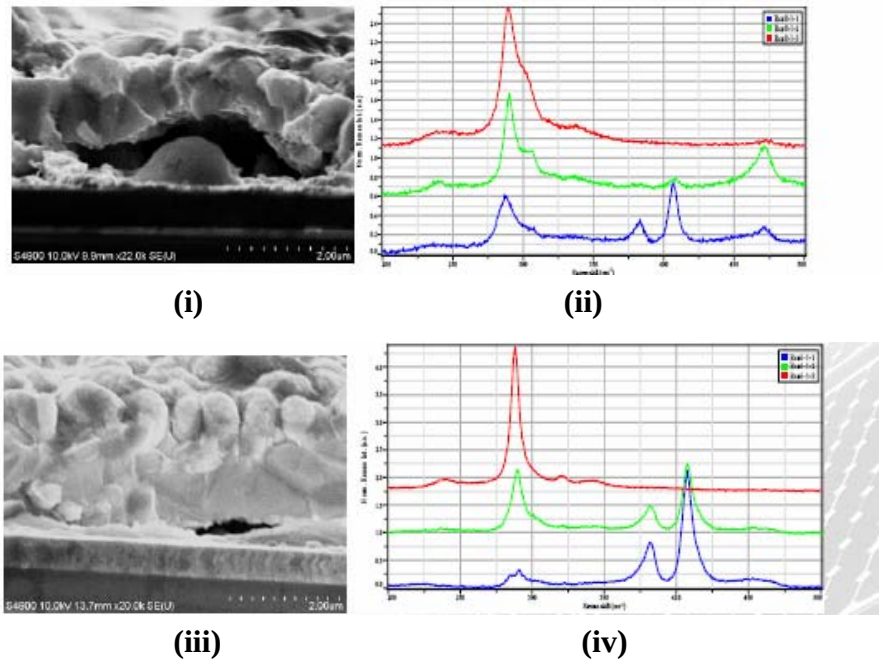

Fig. 40: ***(i)*** *Cross section of a part of the edge of a 15x15 cm^2 cell observed by FEG-SEM (**ii**) Raman spectrum of a part of the edge of a 15x15 cm^2 cell (**iii**) Cross section of a part of the center of a 15x15 cm^2 cell observed by FEG-SEM (**iv**) Raman spectrum of a part of the center of a 15x15 cm^2 cell*

In spite of the edge effect, modules of 15x15 cm^2 surface with an average efficiency of 6.2 % are produced. The open circuit voltage is 1.27 V, the current density is 11mA.cm^{-2}, the fill factor is 44.3%, the maximal power furnished is 733.8mW. Fig. 41-i is a view of a module with the performance just announced.

Fig. 41: Photography of a 15x15 cm^2 module

First steps on 30 x 60cm^2

The upscaling on larger size (i.e. 30x60 cm^2) has already started by the production of molybdenum and ZnO by sputtering. To follow that development, first electrodepositions of Cu on Mo/glass has been performed in the 30x60 cm^2 reactor. Fig. 42 shows a picture of a 30 x 60 cm^2 electrodeposited copper layer on Mo/glass with 6% a standard deviation.

Fig. 42: Photography of a 30x60 cm^2 electrodeposited layer of Cu/Mo/glass with 6% of standard deviation.

Overview

Nexcis develops in parallel two approaches : coelectrodeposition and stack.

The coelectrodeposition is a promising way because synthesis is made from a single bath. Reproducibility and homogeneity in chemical composition, phase distribution and thickness control have been proven for 30 x 30 cm^2. The solutions to be implemented are the optimization of chemistry with in situ control and new concept of furnace.

At the moment a sequential approach seems to be more compatible (well known chemistries with established maintenance procedure, annealing temperature below 550°C) to an industrial processing. The full process sequence has been completed up to an area of 15cm x15cm.

For larger size, homogeneity and reproducibility have to be addressed. This will be assessed with the next generation of equipment (electrolytic bench and furnace) and will be available at the beginning of 2010.

To conclude, results over 8% efficiency on 15 x 15cm^2 have been demonstrated: the reproducibility and homogeneity have to be demonstrated. Furthermore, some 30 x 60 cm^2 steps are internalised: back contact, electrodepostion and target window. A concept of a new 30 x 60 cm^2 furnace has been defined and will be available at the beginning of 2010.

Next steps are the consolidation of 8% on 30 x 60 cm^2 scale (beginning of 2010), the enhancement of efficiency up to 10% via Ga insertion in the precursor and the transfer of procedures from glass to metal substrates.

1.2.4.3 Progress over the whole project duration

The LARCIS project has been extremely important in the understanding of the scalability of the electrodeposition step. This step is really difficult to control and the studies have been focused on: analysis and control of the electrolyte, influence of Mo resistivity and the control of mass transfer phenomena in the bath. This comprehension has given the opportunity to develop a process on larger size of photovoltaic cells from 5 x 5 cm^2 to 30 x 30 cm^2.

Simultaneous researches on Ga insertion have been intensified and the results presented previously have proven the availability of the new procedure.

Analysis and control of the electrolyte

For industrial applications the electrolyte needs to be regenerated after each electrodeposition step. The difference of concentration before and after an electrodeposition is determined by ionic chromatography. The solution is used several times and has to be stable to reproduce the same electrodeposition. Fig. 43 shows the evolution of concentration of the 3 elements [CuII],[InIII],[SeIV] after regeneration on more than 20 runs of deposition on 30 x 30 cm^2. It is easy to validate the fact that the electrolyte is stable and the standard deviation of concentration for the 3 elements are (Cu ± 2,7%, Se ± 3,8%, In ± 2,3%).

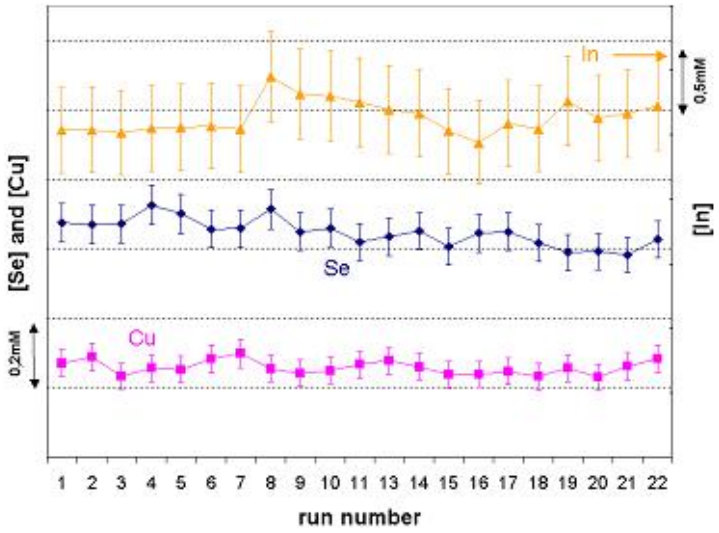

Fig. 43: Evolution of concentration of [CuII],[InIII],[SeIV] after regeneration. Each regeneration follows an electrodeposition on a 30x30 cm^2 cell.

Mo/glass conductivity

In order to have a good homogeneity of composition and thickness of the $CuInSe_2$ precursor, it is important to complete the understanding of bath stability control with the study of resistivity of the substrate of Mo/glass. The role played by the substrate is illustrated on the Fig. 44. The higher the resistivity is, the less homogeneous the composition and the thickness are. The resistivity induces electrical losses on the surface (Fig. 44-ii). It was found that molybdenum layers with sheet resistance ≤ 0.25Ω□ are applicable.

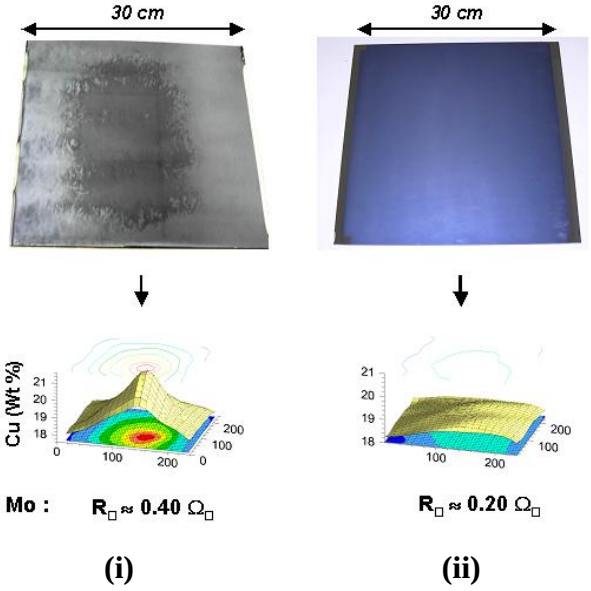

Fig. 44: Two photographs of $CuInSe_2$ after electrodeposition (top) and the copper distribution after Xray fluorescence analysis (bottom). Two types of 30x30 cm^2 are studied. ***(i)*** *Sheet resistance= 0,40 Ohms.* ***(ii)*** *Sheet resistance = 0,20 Ohms.*

Mass transfer phenomena

The mass transfer phenomena have been studied by developing a new concept of electrodeposition reactor using a comb like system (Fig. 45). The innovation was to monitor the homogeneity of composition and thickness only with the dimensions and the stirring system of the reactor.

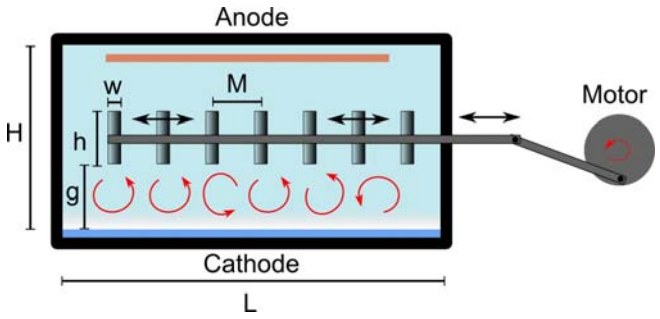

Fig. 45: Electrodeposition reactor based on a comb like system

An adimensionnal number K was defined. This number includes the proximity ration to represent eddy interaction length, the stroke and the Reynolds number.

Experiences performed with the CuNi system are presented on the Fig. 46. The standard deviation of thickness depends on k. It is obvious to conclude that to obtain the less standard deviation, K has to be high.

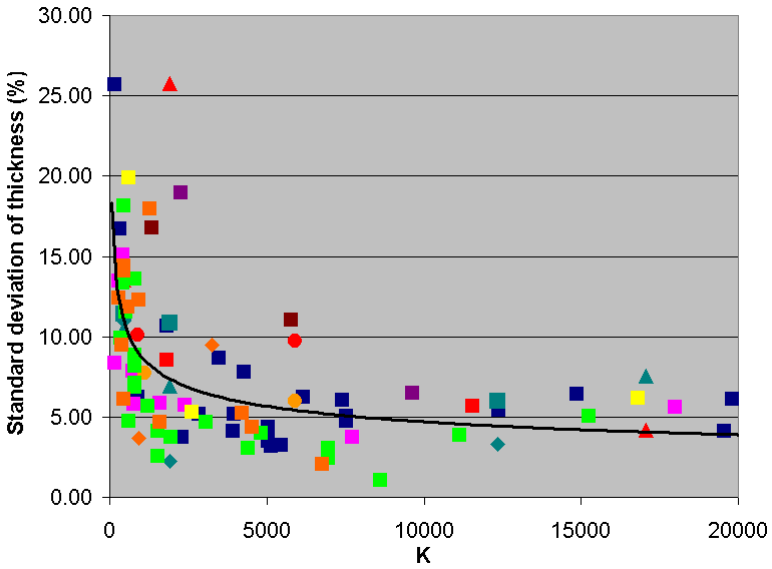

Fig. 46: Evolution of standard deviation of CuInSe2 after electrodeposition as a function of K value

The current density of electrodeposition plays a key role in the control of composition. The Fig. 47 presents the evolution of the equivalent diffusion layer as a function of K.

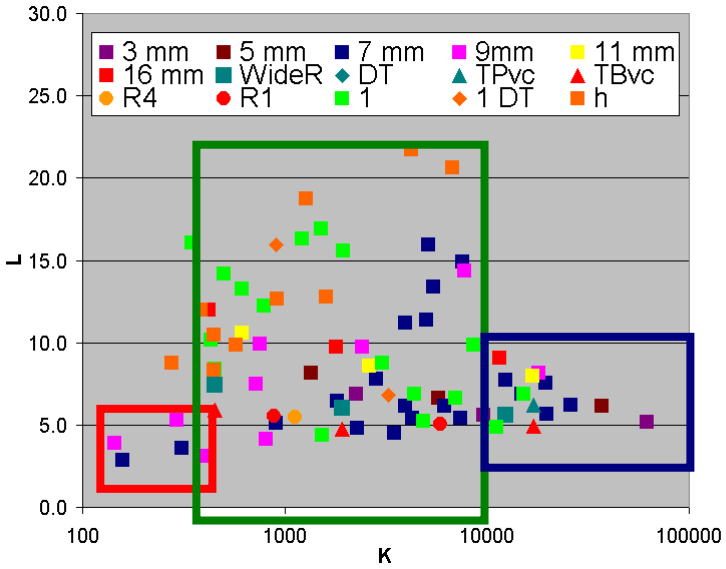

Fig. 47: Evolution of the equivalent diffusion layer as a function of K value

We distinguish 3 regions of K value. For K< 500 and 10000<K<100000, the equivalent diffusion layer is small. For 500<K<10000, the equivalent diffusion layer takes a lot of values, it means that it is possible to choose in this region different deposition growth rate and still have good homogeneities.

Conception and construction of a working 30 x 60cm^2 electrodeposition reactor

A reactor able to deposit $CuInSe_2$ on Mo/glass cells of 30x60 cm^2 has been developed. The photograph is shown in Fig. 48.

Fig. 48: 30 x 60 cm^2 electrodeposition reactor

Conclusion

The understanding of bath stability, influence of Mo resistivity and mass transfer phenomena has given the opportunity for IRDEP to create a prepilot line production working with two approaches of electrodeposition : codeposition and stack approach and a process on $CuInS_2$ cells. In the fourth period of LARCIS project NEXCIS has presented results on cells from 5x5 cm^2 to 15x15 cm^2 and development of electrodeposition on 30x60cm^2 scale. In spite of inhomogeneity problems the efficiencies are over 8% on 15x15 cm^2 and 6.2 % on module 15x15 cm^2. Next step is to adapt the process on 30x60 cm^2 size of cells.

Simultaneously IRDEP has modified its procedures and has studied Ga insertion by electrodeposition. Results on small size 0.1cm^2 has proven the validity of the new protocole and the best performance of cells is 7.8%, Jsc = 35 $mA.cm^{-2}$, Voc = 375 mV, FF = 60%.

1.2.5 Quality and process control

Introduction: The development of in-situ process control techniques by use of optical methods for large-scale solar absorbers was the main goal of this work package. More precisely, laser-light (LLS) and white-light scattering (WLS) were studied as methods for phase monitoring during the $Cu(In,Ga)Se_2$ coevaporation three-stage process, and for the same purpose Raman scattering for the electrodeposited $CuIn(S,Se)_2$ absorbers, where Raman signals during both, the electrodeposition of $CuInSe_2$ and the rapid thermal annealing in sulfur atmosphere, were recorded and evaluated.

1.2.5.1 Laser-light and white-light scattering

The LLS setup used for controlling the In-Se and Ga-Se layer thicknesses of the sequential Ga-Se/In-Se deposition during stage 1 and for detecting the end point (where the [Cu]/([Cu]+[In]+[Ga]) ratio is considered to be about 0.5) was enhanced substantially during the course of the LARCIS project. In addition, the WLS technique was developed and established as process control complimentary to LLS. It has been turned out as particularly useful to record not only the diffuse reflection from a monochromatic light source but also the direct reflection from a white light source. A notable improvement of the monitoring of light-scattering signals was achieved by applying a CCD camera, resulting in spatially resolved information on the reflectance from the surface of the growing layer. By combining LLS and WLS, the phase of the growing layer can be determined from the LLS and WLS signals at any point during stages 1 and 2 of the $Cu(In,Ga)Se_2$ three-stage process.

The CCD intensity exhibits a decay during the last part of stage one of the three-stage Cu(In,Ga)Se$_2$ coevaporation process, which was fitted by an exponential function (Fig. 49). By comparison of the exponential decay parameter α with the integral Ga concentration (measured by means of X-ray fluorescence analysis) for more than forty processes, a linear relationship of α and the Ga concentration was found. Thus, knowing the Ga concentration after stage one, deviations from a certain concentration value may be compensated during the third stage (during which Ga, In and Se are coevaporated).

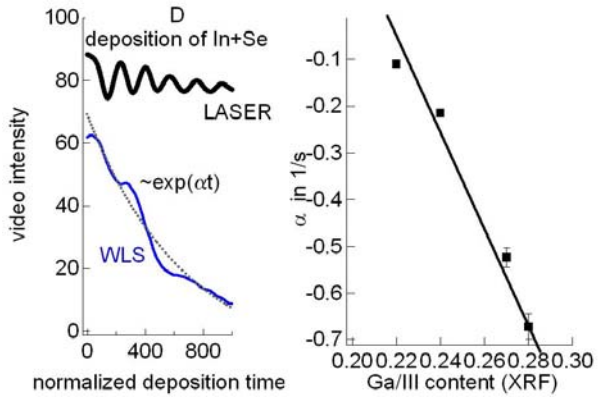

Fig. 49, left: The total white-light intensity vs. the deposition time during the last part ("D") of stage one. As a guideline, the laser-light signal is also shown. The deposition time is normalized to a standard length of 1000. Right: The exponential decay parameter α vs. Ga concentration measured by X-ray fluorescence analysis, showing a linear dependency.

A number of break-off experiments during the second stage were performed in order to investigate the crystal structures and compositions of the In-Ga-Se and Cu-In-Ga-Se layers and correlate these properties with the corresponding LLS and WLS signals (Fig. 50).

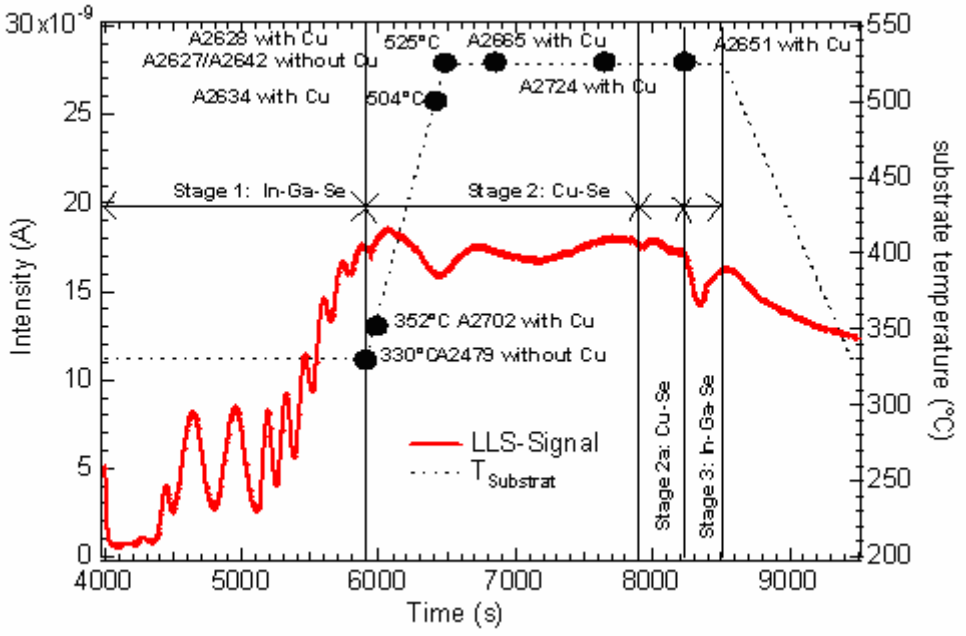

Fig. 50: LLS signal and temperature profile during the three stage process for Cu(In,Ga)Se$_2$. The points on the temperature profile show the break-off positions.

The first stage of the three stage process at HZB consists of a sequenced deposition of Ga-Se/In-Se/Ga-Se/In-Se in order to control the Ga content in the layer. Such a sequence is not feasible for industrial production. Therefore, the influence of the sequenced first stage with respect to LLS and WLS signals was to be investigated. The samples prepared (A2479, A2634, A2642 and A2628) during the temperature ramp were analysed by scanning electron microscopy (LEO GEMINI 1530 FEG) and energy-dispersive X-ray spectrometry (Thermo Noran at 7 kV). The results from Fig. 51 show the influence of the temperature and the enhanced interdiffusion of the Ga and In for higher substrate temperatures. Ga/In gradients in the In-Ga-Se layers are well detectable.

A similar investigation was performed for the copper containing samples (A2642 and A2628, see Fig. 52). In contrast to the In-Ga-Se layers, the elemental distributions of the copper-containing samples show nearly homogeneous distributions of In and Ga. Due to the fact that for all samples studied, the In-Se/Ga-Se layers were deposited sequentially during the first stage, the strongly reduced Ga gradients indicate that it is not important whether the In-Ga-Se precursor is coevaporated (not showing any Ga/In gradients) or deposited sequentially (exhibiting Ga/In gradients). Any Ga/In gradients present after the first stage would be strongly reduced as soon as Cu is introduced into the layers, provided the temperature during the second stage is sufficiently high (above 500 °C).

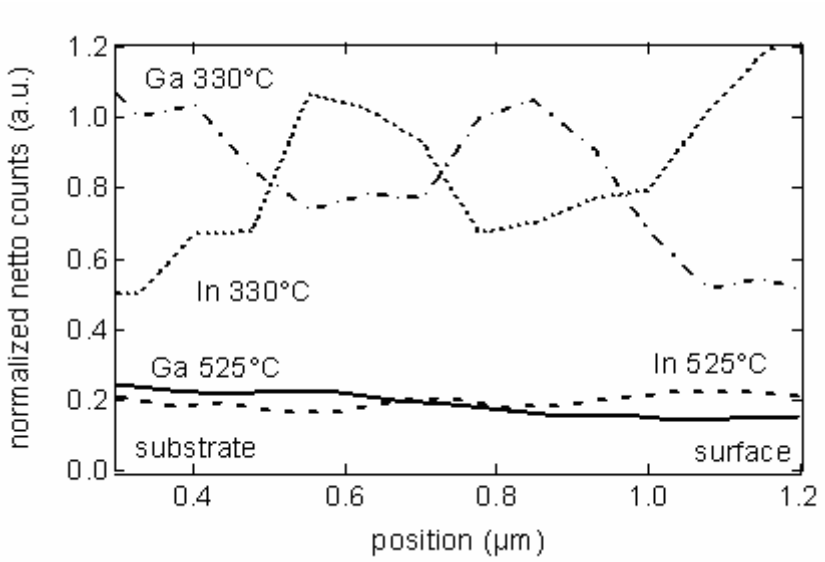

Fig. 51: Normalized distributions of In and Ga in In-Ga-Se layers annealed to various temperatures.

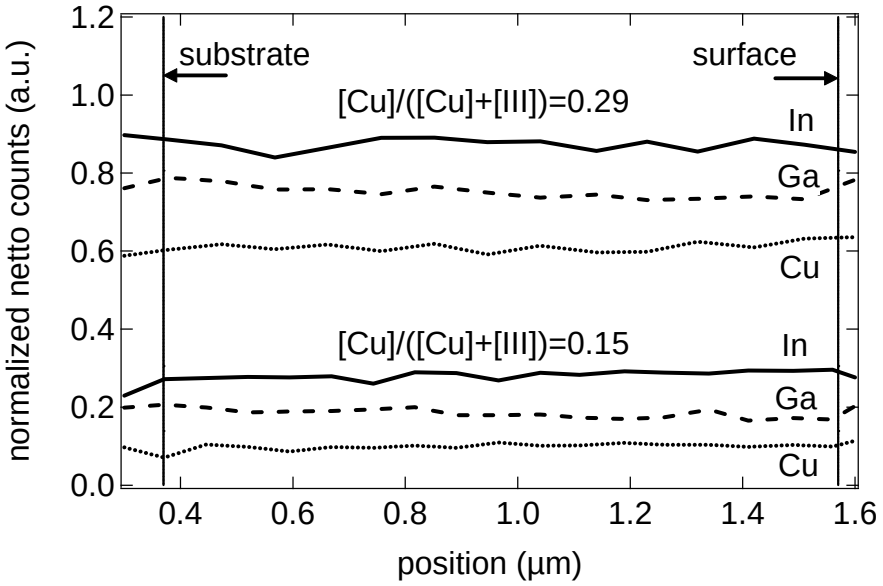

Fig. 52: Normalized distribution of Cu, In, and Ga in Cu-In-Ga-Se samples. Sample A2642 exhibits a [Cu]/([Cu]+[III]) ratio of 0.15, sample A2628 a ratio of 0.29.

The structural investigations of the samples from the break-off experiments during the second stage aimed for two main goals. First, the presence of solid solutions of In_2Se_3 and Ga_2Se_3 was studied. Second, the WLS signals recorded during the second stage were correlated with the results from structural analyses in order to reveal possible phases present. The crystal structures were investigated by means of grazing incidence X-ray diffraction (GIXRD) in a Panalytical X'Pert diffractometer with a Cu Kα source.

These GIXRD results give rise to the conclusion that while mostly γ-In_2Se_3 is present in the top region of sequentially grown In-Ga-Se layers at 330 °C, the annealing to 450 °C or even to higher temperatures leads to an interdiffusion of Ga and In, resulting in the presence of a $(In,Ga)_2Se_3$ solid solution. The corresponding elemental distributions are illustrated in Fig. 51.

The XRD measurements in comparison with the WLS signals (Fig. 53) demonstrate the great potential of the LLS/WLS process control. The appearance of the ordered vacancy compounds (OVC) is detectable by a decrease in the WLS signal (increased roughness of the layer). The formation of copper selenides is related to a strong increase of the WLS signal, which can be related to enhanced direct reflection of these metal-like compounds.

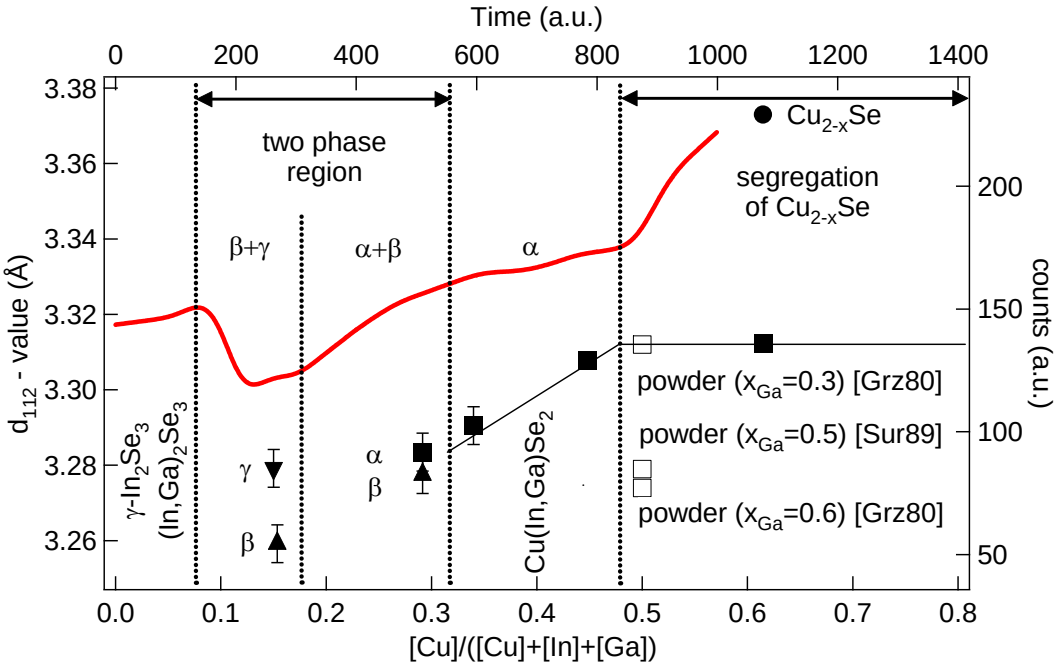

Fig. 53: Extracted 2-theta values of 112 peaks vs. Cu content in the Cu-In-Ga-Se, from GIXRD measurements on samples from break-off experiments during the second stage. Cu-In-Ga-Se phases present are highlighted: $Cu(In,Ga)Se_2$ (α), $Cu(In,Ga)_3Se_5$ (β) and $Cu(In,Ga)_5Se_8$ (γ).

It is shown that by structural and compositional analyses of In-Ga-Se and Cu-In-Ga-Se layers from break-off experiments during the second stage of the $Cu(In,Ga)Se_2$ three-stage process, increasing and decreasing WLS signals monitored during this stage can be related to phase transformations of between the In-Ga-Se and Cu-In-Ga-Se compounds as well as to the beginning of the formation of Cu-Se. Further studies will be aimed to reveal the importance of the presence of Cu-Se on the recrystallisation of the Cu-In-Ga-Se and to the reactions taking place during the third stage (In-Ga-Se coevaporation).

The analyses and understanding of the LLS and WLS signals obtained during stage 3 should be object of future studies in order to obtain eventually the means for a self-consistent growth control for the complete three-stage process.

It is noteworthy that the LLS setup was transferred successfully from the stationary coevaporation chamber for small-scale samples at HZB to the 30x30 cm^2 in-line deposition system at ZSW. I.e., it is demonstrated that all the development of the LLS and WLS techniques performed for fundamental research in the laboratory may be eventually applied in industrial $Cu(In,Ga)Se_2$ growth systems, and therefore it will be very useful for the rapidly growing photovoltaic industry.

A patent on "METHOD FOR THE IN-SITU DETERMINATION OF THE MATERIAL COMPOSITION OF OPTICALLY THIN LAYERS, ARRANGEMENTS FOR PERFORMANCE AND APPLICATIONS OF THE METHOD" was registered with the Publ. No. WO/2009/012748.

1.2.5.2 Raman scattering

ED process - Characterisation of electrodeposited $CuInSe_2$ precursors

In-situ measurements $CuInSe_2$ (CISe) precursors were performed using a BWTek modular system with fibre optics coupling. The system includes a BTC-161-E spectrometer, a BAC 101 Raman probe specially designed to stand the acidic conditions of the electrolyte and a 785 nm solid state laser coupled to the measuring probe.

Measurements were made with the probe immersed in the electrolyte, using a scaled-down cell that was specially designed for testing of in-situ measurements (volume ~ 250 ml, magnetic agitation). The interpretation of the spectra measured as function of time during the electrodeposition (ED) process has been made by analysing the evolution of their integral intensity at the different regions where the contributions from the main phases detected in the layers appear. These correspond to the OVC (150 cm^{-1} spectral region), chalcopyrite ordered $CuInSe_2$ (CISe, 170 cm^{-1} spectral region) and Se-related secondary phases (elemental Se + Cu-Se binaries, 240 cm^{-1} spectral region).

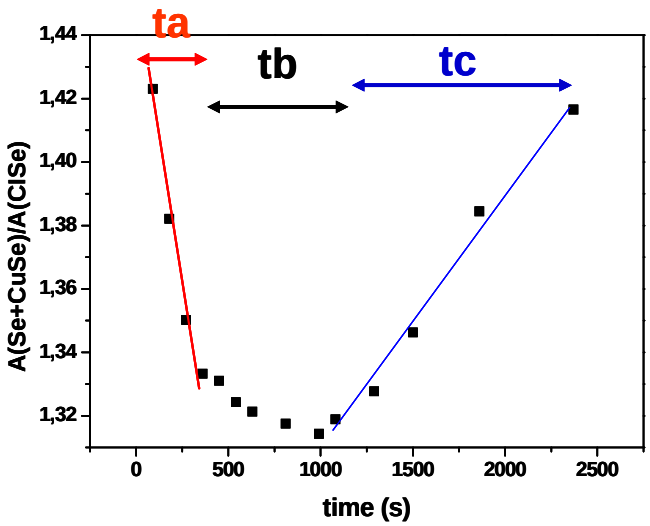

Fig. 54: Relative integral intensity of [Se + (Cu-Se)] phases in relation to the main CISe one versus ED time

Fig. 54 shows the evolution of the relative integral intensity of [Se + Cu-Se] phases in relation to that of the main CISe one versus time. These measurements show the existence of three different stages in the ED growth of the layers:

Initial stage with the highest contribution of (Se+Cu-Se) phases (labelled t_a in Fig. 54). This is related to the existence of a preferential growth of Se and (likely) Cu rich Cu-Se phases, that takes place at the initial growth stage. Just after the initial measurements there is a strong decrease in the relative contribution of the Se-related secondary phases, and the system evolves towards the following (intermediate) stage;

Intermediate stage (labelled t_b in Fig. 54): at this stage the relative spectral contribution from Se-related secondary phases has the lowest value, and remains almost constant with time. This corresponds to a preferential growth of the main CISe phase;

Final stage: for longer deposition times (≥ 1000 s, for the used ED conditions) there is a further increase in the relative the spectral contribution from (Se + Cu-Se) secondary phases. This corresponds to the formation of elemental Se and $Cu_{2-x}Se$ precipitates identified by

surface Raman scattering and XRD measurements [*V. Izquierdo-Roca et al, Physica Status Solidi (a)* ***206*** *1001 (2009)*].

This behaviour agrees with the preliminary ex-situ analysis of the ED process, reported in [*V. Izquierdo-Roca et al, Surface and Interface Analysis* ***40*** *798 (2008)*] In this previous work, the Raman scattering analysis of layers grown with different times showed the existence of a maximum contribution from elemental Se in the spectrum from the thinnest sample (thickness about 40 nm). The absence in this spectrum of a significant contribution from Cu-Se phases suggests the formation at the initial growth stages of Cu-rich phases with very low Raman efficiency, as Cu_2Se. This is also supported by the ex-.situ chemical analysis of the layers reported in [*E. Saucedo et al. Thin Solid Films, in press (2009)*]

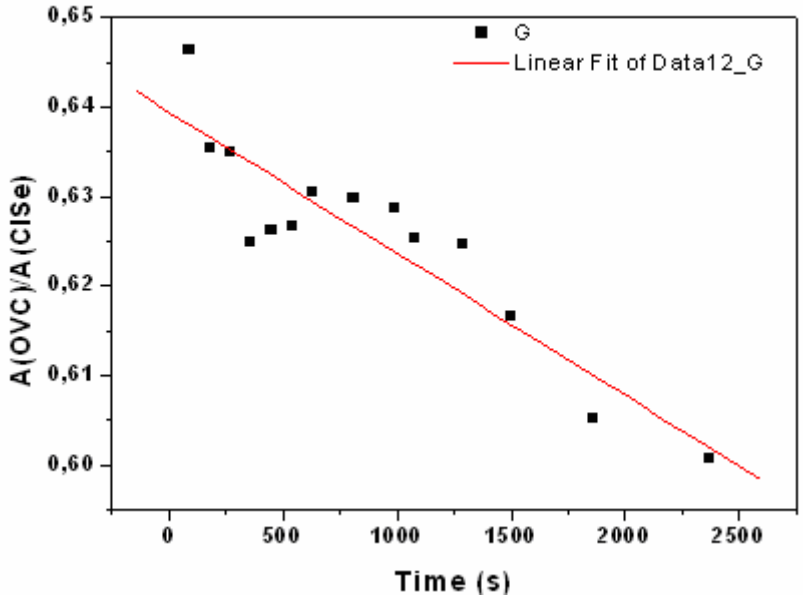

Fig. 55: Relative integral intensity of the OVC phase in relation to the main CISe one versus ED time. Full line is a linear fitting of the data

In addition, the analysis of the spectra measured at real time conditions during the ED growth of the layers gives also information related to the evolution of the OVC phase. Preliminary ex-situ measurements were strongly compromised by the high level of noise in the determination of the relative integral intensity of this contribution. The much higher number of measurements obtained at in-situ conditions has allowed the observation of a clear trend in these data, in spite of the noise, as shown in Fig. 55. These measurements point out the existence of a maximum OVC contribution at the initial growth stages, and for longer times the relative intensity of this phase tends to decrease with growing time. This agrees with the preferential incorporation of Cu in Cu rich Cu-Se phases at the initial growth stages, that would lead to a Cu deficiency in the synthesised chalcopyrite phases. This would explain the presence in the ED precursors of the Cu poor OVC phase, in spite of the overall Cu excess conditions used in the ED growth.

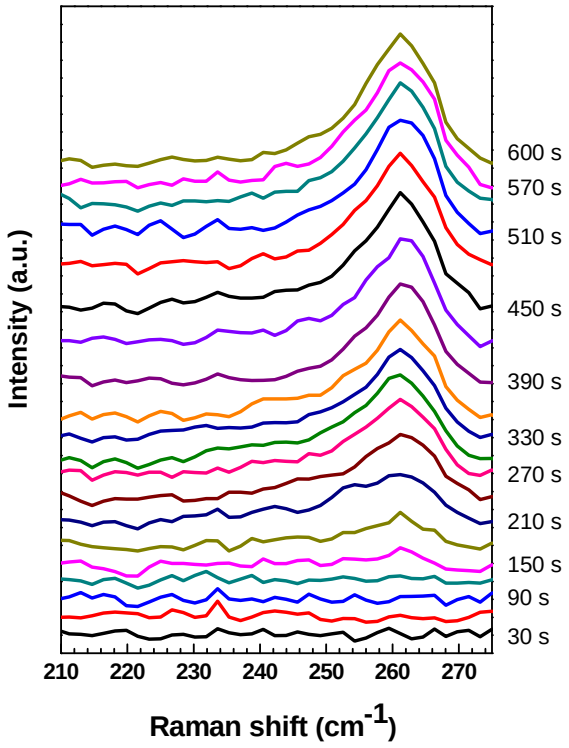

Fig. 56: Real-time Raman spectra measured under electro-less growing conditions. Spectra were subtracted from the water spectral contribution from the aqueous electrolyte. The spectra measured at different times after immersion of the Mo coated glass substrate in the electrolyte are vertically shifted.

On the other hand, and in order to clarify the possible existence of electro-less processes affecting the initial ED stages, in-situ Raman spectra have also been measured with the electric terminals in open circuit conditions. In Fig. 56 are plotted the spectra measured in the 210-280 cm^{-1} region at different times after immersion of the Mo coated glass substrate in the electrolyte, after subtraction of the signal from the aqueous electrolyte. This figure shows the gradual appearance of the Se-Se vibrational mode characteristic of a Cu-Se phase at about 260

cm^{-1}. The plot of the integral intensity of the mode versus the measuring time (shown on Fig. 57) suggests the presence of three different dynamical regimes:

Stage (a) is characterised by the absence of a significant Raman signal. This could be related to the formation of Cu rich phases with very low Raman efficiency (as Cu_2Se), This would be supported by the higher diffusivity of Cu ions in relation to the Se ones in the electrolyte;

Stage (b): formation of a $Cu_{2-x}Se$ phase; and

Stage (c); the drastic change in the growth rate suggests the formation at this stage of a different phase, as CuSe.

These data suggest that formation of the Cu- rich phases at the initial ED stages is related to the existence of an electro-less process affecting the initial growth conditions. Further analysis (by complementary ex-situ AES/XPS and XRD measurements) is required to clarify this behaviour.

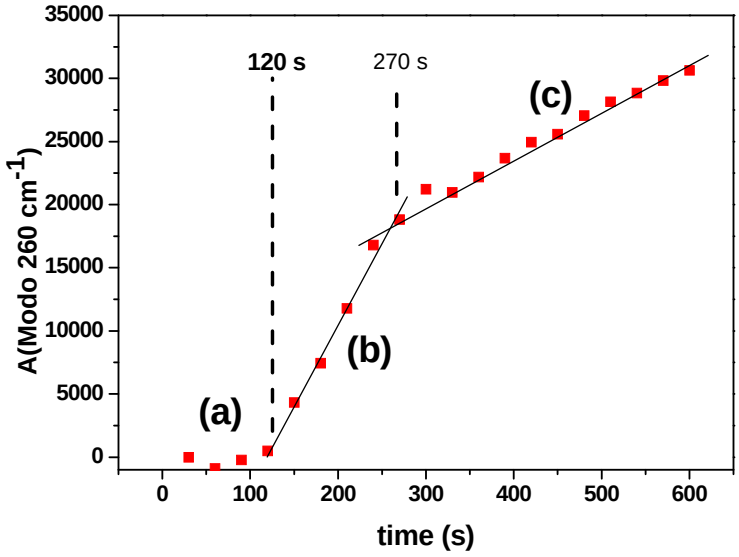

Fig. 57: Integral intensity of Se-Se mode from the spectra shown in Fig. 56 vs time

Raman scattering analysis of PVD absorbers

Raman scattering based techniques have also been applied to the surface and in-depth resolved characterisation of absorbers synthesised by PVD based processes. This has included the surface and in-depth resolved analysis of secondary phases in Cu-poor $CuInSe_2$ (CISe) based thin films, as function of the Cu/In content ratio, in collaboration with ZSW. This study is reported in [*X. Fontané et al, Appl. Phys, Lett.* ***95*** *121907 (2009)*].

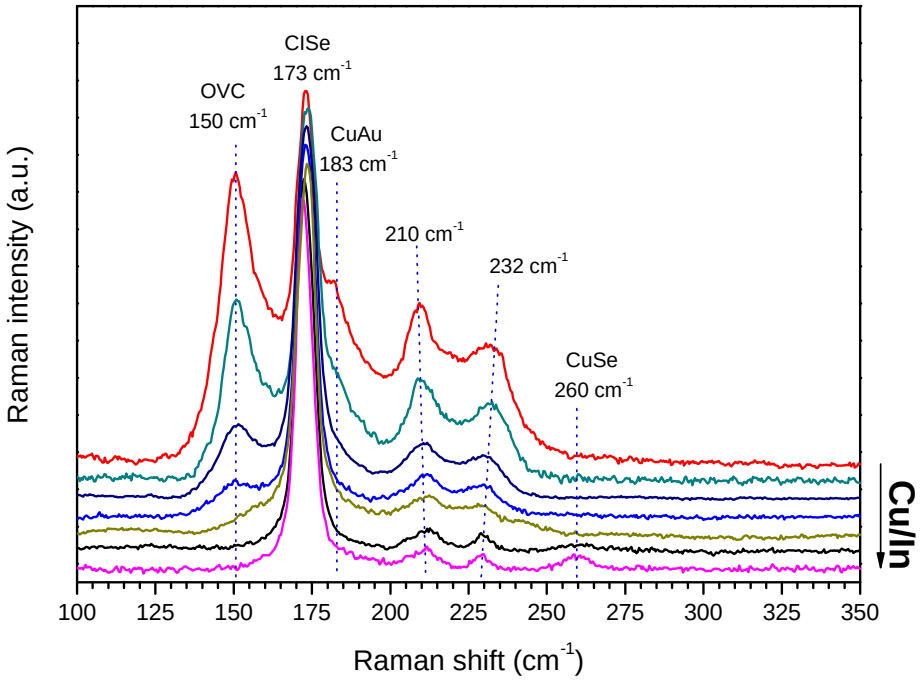

Fig. 58: Raman spectra from the surface of samples with different Cu/In content ratio, normalized to the intensity of the A_1 mode from chalcopyrite ordered CISe

Fig. 58 shows the Raman spectra measured on the surface of CISe layers grown with Cu/In content rations between x = 0.48 and x = 1.14. These measurements were made using the Horiba-Jobin-Yvon T64000 spectrometer available at the UB-EME group, with an Ar^+ laser excitation source (514.5 nm) under macroscopic measurement conditions (size of laser spot on surface of the samples about 100 μm, excitation power 20 mW). The samples were grown by an inline coevaporation process on Mo coated glass substrates.

These measurements show the formation of the OVC phase in the range of compositions corresponding to $x \leq 0.82$. This is indicated by the presence of a peak in the 150-160 cm^{-1} spectral region that has been identified with the most intense A_1 symmetry mode from OVC [*Ch.-M. Xu et al, Semicond. Sci. Technol.* ***19*** *1201 (2004)*]. This mode coexists with the main peak characteristic of chalcopyrite (CH) ordered $CuInSe_2$ at about 173 cm^{-1}. For values of $x \leq 0.66$, the spectra also show a contribution at about 183 cm^{-1}, arising from the A_1 dominant band of CuAu-ordered $CuInSe_2$ [*J. Álvarez-García et al, Phys. Rev. B.* ***71*** *054303 (2005)*]. These results indicate the coexistence of the OVC, CuAu ordered $CuInSe_2$ and chalcopyrite (CH) ordered $CuInSe_2$ phases, as function of the Cu content in the layers. Finally, increasing the Cu content to values of $x \geq 0.92$ leads also to the appearance of the Se-Se vibrational mode at about 260 cm^{-1}, which is characteristic for Cu-Se binary phases.

In order to clarify the presence of the OVC phase inside the layers, Raman spectra were measured with a Raman microprobe focusing the laser spot at different positions on the cross-section of the layers. These measurements were performed with an Olympus metallographic microscope coupled to the T64000 spectrometer, and the measured spectra were compared with those directly measured on the front and back surface of the layers, after mechanical removal of a piece of the layer from the substrate.

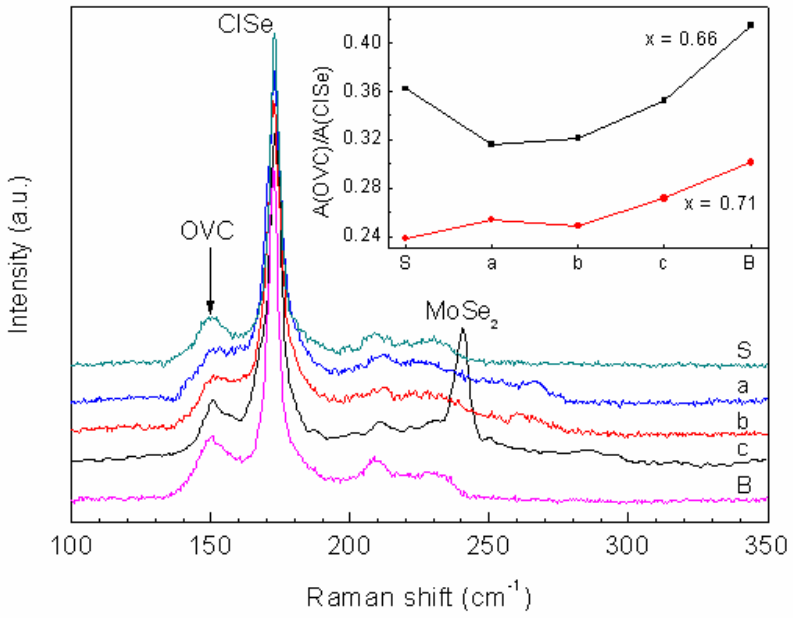

Fig. 59: Micro-Raman spectra measured with the laser spot focused at different positions from the cross-section of the layer with x=0.66:(a) surface region, (b) mid region, and (c) back region, together with those directly measured from the front (S) and back (B) surfaces. The spectra are normalized to the intensity of the main CH-CISe mode. Inset in the figure shows the evolution of the relative integral intensity of the OVC mode in relation to the CH-CISe one from samples with x=0.66 and x =0.71, as deduced form the fitting of the corresponding spectra.

Fig. 59 shows the spectra measured with the laser spot focused at different positions on the cross-section of the sample with x=0.66, together with those directly measured from the front and back surfaces. For the spectra measured on the cross-section of the layers, the thickness of the region contributing to the spectra is determined by the size of the laser spot. For the used experimental conditions (X100 objective, 514.5 nm excitation wavelength), the estimated spot size is about 0.7 μm. Moving the laser spot towards the back region leads to the appearance in the spectra of a peak at 240 cm^{-1} that has been identified with the main vibrational mode from $MoSe_2$.

All the spectra in Fig. 59 are characterized by the presence of a clear contribution in the OVC spectral region. The inset in the figure shows the plot of the relative intensity of the OVC peak in relation to that of the CH-CISe mode as derived from the fitting of the spectra measured at different positions from the samples with x=0.66 and x==0.71, respectively. In the first case (x = 0.66) the spectra directly measured on the front and back surfaces show a higher relative intensity of the OVC mode, which suggests the existence of a higher relative content of this phase at these regions. The highest intensity of the mode measured from the back surface would be related to a higher enhancement on the occurrence of the OVC phase at the region close to the back interface. Increasing the content of Cu (x =0.71) leads to an overall decrease of the relative intensity of the OVC mode, and also affects its in-depth distribution: in this case there is only a maximum on the relative intensity of the mode at the back interface region. These data suggest a significant role of the $CuInSe_2$ /$MoSe_2$ interface on the formation of the OVC phases that would result in an enhancement in the occurrence of these phases at the back interface region. Presence of secondary phases at the back interface

region may have a special relevance because of their potential impact on the electrical characteristics of the back contact in the cells.

In-depth resolved measurements have also been made to analyse the in-depth gradual distribution of Ga in double graded Cu(In,Ga)Se_2 (CIGS) layers developed by the EMPA group. These measurements are reported in [*X. Fontané et al, Appl. Phys Lett (in press) (2010)*]. In-depth resolved analysis of the frequency of the main CIGS Raman mode in the spectra measured after sputtering of the layers at different depths lead to identification of different compositions across the layer thickness. The obtained data are in good agreement at both qualitative and quantitative levels with the in-depth resolved composition analysis of the samples by sputtered neutral mass spectroscopy. In addition, Raman measurements have also allowed the detection of additional phases as OVC at the surface region of the layers.

Sulfurised samples: Analysis of electrodeposited absorbers.

The activities performed at the level of the absorbers (after the sulphurisation step) have allowed to achieve a good level of knowledge on the main microstructural features characteristic of the structures fabricated with these processes, and their dependence on processing parameters as the sulphurising temperature and time.

Among the most interesting results, first data have been reported on the synthesis by ED processes of $CuIn(S,Se)_2$ absorbers with gradual in-depth composition. This has revealed the potential of Raman microprobe measurements tools for the in-depth resolved analysis of non-homogeneous complex layers. In-depth resolved measurements performed on different kinds of layers (synthesised using both ED and PVD processes) has allowed to corroborate the ability of Raman scattering based techniques for the characterisation of complex $Cu(In,Ga)(S,Se)_2$ layers with non homogeneous in-depth composition, and for the detection of surface and/or interficial phases in these layers (OVCs, MoS_2, $MoSe_2$...).

On the other hand, the analysis of the Raman spectra from a wide range of absorbers produced through the duration of the project has allowed observing a correlation between the FWHM of the main A_1 CIS Raman peak and V_{oc}, being this parameter proposed as quality indicator for the process. Finally, measurements performed under quasi-resonant conditions have shown their ability for the non destructive fast monitoring of the absorber composition.

1.2.6 Technological and economical assessment

Introduction: The purpose of this work package was to evaluate the maturity of processes developed under the LARCIS project as well as to asses the potential of the respective processes in terms of technology and business. The main objectives were:

- to asses the project development with respect to yield, material consumption, throughput and commercial module performance
- to develop a common cost estimation methodology both for the co-evaporation and electrodeposition CIS approach
- to estimate electrodeposition and co-evaporation cost production

1.2.6.1 Description of work

Representatives from the commercial CIS producing partners Würth Solar (WS), Electricité de France (EDF), Solibro and the glass coater Saint Gobain Recherche (SGR), formed a committee which analyzed the achievement within various tasks and work packages with respect to the objectives and milestones reached.

The assessment criteria were the achieved (or estimated) yield, material consumption, throughput and the commercial module performance. In the course of the project, SGR reconsidered their participation in the work package and did not contribute to the manufacturing costs estimation.

1.2.6.2 Project development assessment

The first objective was to assess the project development in terms of yield, material consumption, CAPEX and commercial product performance. It was agreed that the following processes and achievements are mature enough to make meaningful assessments:

- deposition of the ZnS based buffer layer by CBD (CBD-ZnS)
- deposition of an In_2S_3 buffer layer by evaporation (Evap. In_2S_3)
- graded CIGS deposition process
- thin CIGS
- CIGS deposition by electrodepostion
- modified molybdenum layer

The assessment of the development and performance of the listed processes and achievements is a result of a discussion between all partners. The development and performance of a process or achievement was assessed by comparing them with today's standard process (2 µm PVD deposited CIGS + CBD CdS). For the assessment a grading scale comprising three grades, i.e. low, normal and high, was used. The grades represent a relative level of a process development in respect to the today's standard process. Some processes received an additional grade (separated from the first degree by a slash mark) relating to its future potential. The results of the evaluation are summarized in Tab. 8.

Tab. 8: Development of the achievement of particular task and WP's in respect to the today's production process. The first grade gives an estimation of the status of the present process, and the second (after the slash mark) – an estimation of the future potential of the process.

Process	Yield [Low/Normal/ High]	Material consumption [Low/Normal /High]	CAPEX [Low/Normal/ High]	Efficiency [Low/Normal/ High]
CBD-ZnS	Low/Normal	Higher	Higher	Equal/High
Evaporated In_2S_3	Normal/Very Good	Lower	Lower	Lower/High
graded CIGS process	Normal	Equal	Higher	High

Thin CIGS	Normal	Lower	Equal/Lower	Lower
Electrodep. CIGS	Normal	Lower	Lower	Lower/Equal
Modified Mo	Normal	Lower	Higher	Lower/High

1.2.6.3 Assumptions for cost evaluation

As a framework for cost estimation, a factory having capacity of 100 MWp/year and yield of 90% is assumed. The factory is supposed to produce frameless modules with dimensions of 60 x 120 cm^2. CAPEX is expressed in €/m^2 and the cost of buildings is excluded from the cost. Any other equipment requirements are included in the equipment cost for the specific process, *i.e.* electrodeposition or co-evaporation process. The assumptions are summarized in Tab. 9.

Tab. 9: The framework for production cost estimation.

Factory	
Production capacity	**100 MWp/year**
Yield	**90%**
Module	
Dimension	**60 x 120 cm^2**
CAPEX	
Expressed in	**€/m^2**
Facility	
Building	**Excluded**
Equipment requirements	**Included in each specific equipment**

1.2.6.4 Evaluation of manufacturing costs

Production cost break-down for different process steps for manufacturing modules containing electrodeposited CIGS and co-evaporated CIGS can be seen in Tab. 10. The table contains relative values in respect to the total cost of the standard CIGS co-evaporation process, represented in the table as 100%. The values represent cost/m².

The estimated cost is expressed by CAPEX, Material costs (Materials) and other costs (Cost). The process steps for which the cost was estimated are: manufacturing of a substrate with a molybdenum layer (Mo/substrate), CIGS absorber deposition process (CIGS), deposition of a buffer layer (Buffer), deposition of a window layer (TCO), scribing processes (P1/P2/P3), back-end processes (Back-end), automation and handling, labour and overheads. For all

process steps, apart from CIGS and Buffer, CAPEX and material cost are combined together and represented by one value. Since the steps of CIGS deposition and substrate manufacturing (Mo/substrate) for co-evaporated and electrodeposited CIGS require different equipment and consume different amount of material, separate CAPEX and material cost estimations are provided for these deposition methods. First value represents the estimation for a process comprising co-evaporation of CIGS and the second, separated by a slash mark, a process comprising electrodeposited CIGS.

As can be seen in Tab. 10, the total cost for electrodeposited CIGS constitute 92% of the co-evaporated CIGS process costs. This difference is due to lower CAPEX and material cost for electrodeposition process. Please note that the total cost of each technology indicated in Tab. 10 is only estimation at 5%, as it may vary depending on a specific industrial process.

Tab. 10: Estimated relative production cost for a module with co-evaporated and electrodeposited CIGS. CAPEX and Material costs for Mo/substrate and CIGS are represented by two numbers, wherein the first number corresponds to CIGS absorber deposition by co-evaporation and the second (after the slash mark) – by electrodeposition. The cost for the remaining process steps is the same for both manufacturing ways. The relative cost represents a percentage of the total cost of manufacturing a module by co-evaporation.

Process step	CAPEX	Materials	Cost	Total
Mo/substrate	11/12			11/12
CIGS	10/4	5/2		16/6
Buffer	4	1		5
TCO	5			5
P1/P2/P3	2			2
Back-end	29			29
Automation and handling	5			5
Labour			19	19
Overheads			9	9
Total				100/92

1.2.6.5 Impact of module efficiency on manufacturing cost

Tab. 11 shows how the cost/Wp (represented by relative values) changes with efficiency for modules comprising co-evaporated CIGS (the left part of the table) and electrodeposited CIGS (the right part). The number marked in red represent the efficiency value for currently available modules. All values in the table are relative in respect to the today CIGS co-evaporation process, which corresponds to 100% cost.

Tab. 11: Module efficiency impact on relative manufacturing cost.

Co-evaporated CIGS		Electrodeposited CIGS	
Efficiency	Relative Cost/Wp	Efficiency	Relative Cost/Wp

8%	157%	8%	136%
9%	140%	9%	121%
10%	126%	10%	109%
11%	114%	11%	99%
12%	105%	12%	90%
12.6%	100%	13%	84%
13%	97%	14%	78%
14%	90%	15%	72%
15%	84%		

1.2.6.6 Module efficiency impact on manufacturing cost

The cost/Wp for a CIGS module is mainly affected by material and equipment costs, as well as efficiency of the module (see Tab. 11). The results accomplished during the LARCIS project influence both material and equipment costs for manufacturing a solar cell module. For example thinner CIGS, electrodeposition of CIGS absorber layer, Cd-free buffer layer and graded CIGS deposition process will affect the final cost/Wp. The impact of a result on efficiency and cost/Wp of CIGS solar module is illustrated in Fig. 60a-c. It is important to note that Fig. 60a-c are not scaled and do not enable direct quantitative comparison of the various progresses. Indeed, they only aim at indicating qualitatively the trends in term of cost reduction and in relation to each process.

At the beginning of the project, the status of the co-evaporated CIGS corresponded to a given efficiency and cost/Wp (the red dot in Fig. 60a). The results of the project which influence the efficiency of the CIGS solar module move the dot along the blue line to the left or to the right on the graph. On the other hand, if a result of the project directly influences the cost of manufacturing a CIGS solar cell, *e.g.* lower material or equipment cost, the status dot moves upwards (higher costs) or downwards (lower costs), and creates a new cost/Wp and efficiency dependency curve parallel to the original one.

The status of the CIGS solar cell/module before the LARCIS project is represented by a red dot in Fig. 60a. During the course of the project, a Cd-free technology was developed. According to the reported results, this process improves the efficiency of CIGS solar module. Thus, the position of the CIGS solar module moves towards higher efficiency and lower cost/Wp (dot A1 in Fig. 60a). In addition, the results form graded CIGS process experiments also show improvement of the efficiency of CIGS solar module. This fact moves the position of the CIGS solar cell/module even further towards higher efficiencies, further decreasing the cost (dot A2 in Fig. 60a).

Another teaching from the LARCIS project is that thinning down the CIGS layer in a solar module lowers the cost of the CIGS absorbing layer deposition but do not improve the efficiency of the CIGS. In this case, the CIGS technology status point moves towards lower cost/Wp but stay at the same efficiency level. This creates a new dependency curve below the original one (the green curve and dot B in Fig. 60b).

During the LARCIS project it was also shown that the electrodeposition of CIGS lowers the material and equipment costs for the absorber layer deposition. This fact moves the status of CIGS technology further down from the starting point and creates a new cost/Wp and efficiency dependency curve below the original line (dot C1 on the grey line in Fig. 60c), progresses in the deposition process along the LARCIS project have increased the efficiency (dot C2 on the grey line in Fig. 60c). What was also learned during the project was that applying a Cd-free layer on the electrodeposited CIGS improves the efficiency of the module. Thus, the status point of electrodeposited CIGS moves rightward, towards higher efficiencies along the curve, further decreasing the cost (dot C3 on the grey line in Fig. 60c).

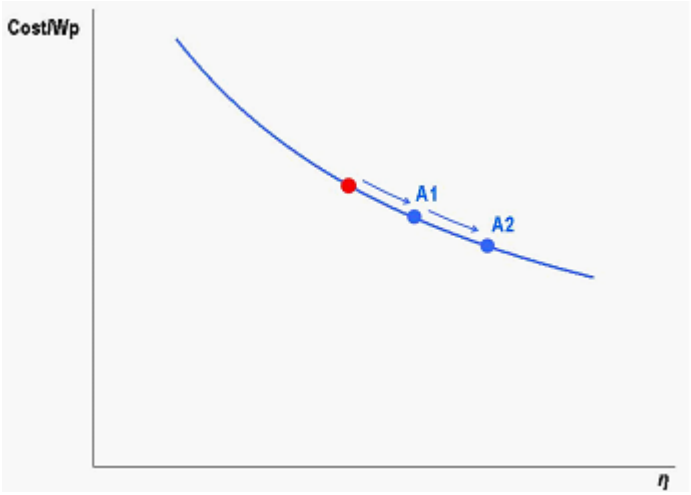

Fig. 60a: Cd-free process moves the CIGS technology status from its position before LARCIS had started (red dot) towards higher efficiency (blue dot A1 in the middle of the graph). Efficiency is further improved by the graded CIGS process (the outmost right blue dot A2).

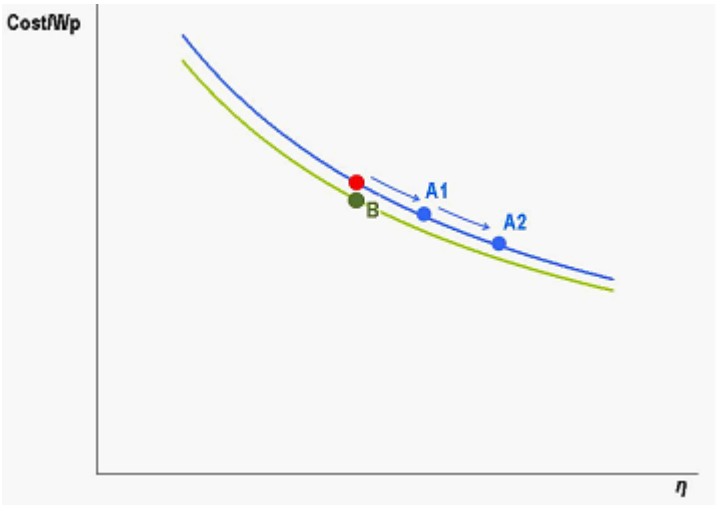

Fig. 60b: Thinning down CIGS absorber layer lowers cost/Wp but do not enhance the efficiency. This moves the CIGS technology before the project (the red dot) towards lower cost and on the new curve (the green dot B on the green curve).

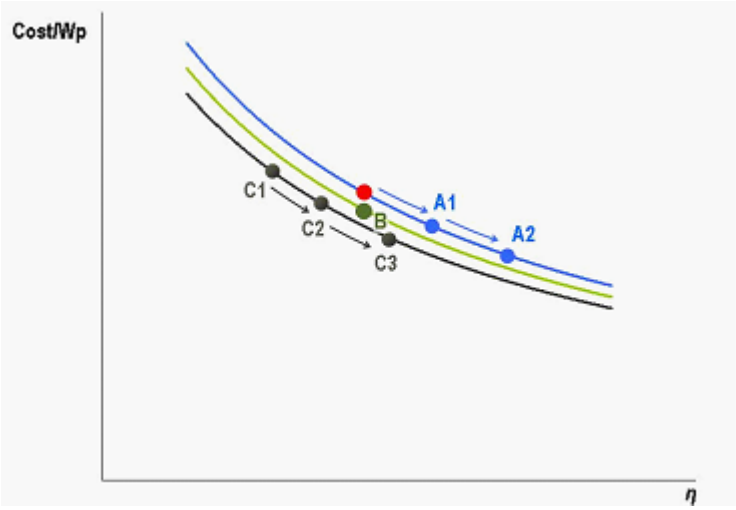

Fig. 60c: Electrodeposition of CIGS lowers cost/Wp and moves the technology status point from its beginning position (red point) to the new position (dot C1) on the new cost/Wp line (grey line), deposition improvement increased the efficiency (dot C2). Cd-free process increases the efficiency further decreasing the cost (dot C3).

2 Dissemination and use

Overview table

Exploitable Knowledge (description)	**Exploitable product(s) or measure(s)**	**Sector(s) of application**	**Timetable for comer-cial use**	**Patents or other IPR protection**	**Owner & Other Partner(s) involved**
1a. Modified Mo back contact	*ZrN/Mo as highly reflective back contact; application of very thin CIGS layers becomes possible*	*CIGS PV industry, preferably members of the consortium*	*not yet planned*	*Patent of Solibro from 2004*	*UU-ÅSC, ETHZ, SGR, ZSW*
1b. Modified Mo back contact	*TiN/Mo back contact for higher reflectivities and stabilities*	*CIGS PV industry, preferably members of the consortium*	*not yet planned*		*EMPA (ETHZ), UU-ÅSC, SGR, ZSW*
1c. Mo back contact on large area with high conductivity	*Mo back contact with high conductivity to be applicable both for the ED CIS processing and the coevaporation approach*	*Supplier of the CIGS PV industry, preferably Saint Gobain Glass (SGG)*	*already produced at SGG*		*SGR, EMPA (ETHZ)*

Exploitable Knowledge (description)	**Exploitable product(s) or measure(s)**	**Sector(s) of application**	**Timetable for comer-cial use**	**Patents or other IPR protection**	**Owner & Other Partner(s) involved**
2a. Cd-free buffer layer based on the combination of a CBD-ZnS and a MnZnO layer	*Chemical/physical recipe and technological know-how on the deposition of a Cd-free effective buffer for CIS based solar cells*	*CIGS PV-manufacturers, i.e. Würth Solar, EDF*	*depends on process qualificatio n on large area*	*patent of ZSW applied in 2006*	*ZSW, CNRS*
2b. Cd-free vacuum buffer based on evaporated In_2S_3	*Deposition method; Cd-free CIGS solar cells*	*CIGS PV-industry, preferably members of the consortium*	*not yet known*	*no*	*HZB*
3a. Inline graded CIGS coevaporation	*Inline CIGS graded coevaporation for higher efficiencies in a production line*	*CIGS manufacturers using the coevaporation method; more efficient large-area modules*	*depends on process qualificatio n on large area*	*no*	*ZSW, Würth Solar*
3b. Coevaporation technique of very thin CIGS absorbers	*Strong reduction of absorber thickness in combination with no or minor reduction of efficiency; cost reduction*	*CIGS manufacturers using the coevaporation method;*	*depends on further progress*		*UU-ÅSC, Solibro, Würth Solar*
4. Electrodeposition of $Cu(InGa)(S,Se)_2$	*Homogeneous ED of CIS absorbers on large areas*	*CIS manufacturers using the ED method; preferably the EDF*	*depends on further progress*		*EDF, CNRS*
5a. Process control of the inline CIS process by laser light scattering and CCD camera	*CIGS production at high yield*	*CIGS manufacturers using the inline coevaporation method*	*depends on further progress*	*patent-registered by the HZB*	*HZB, ZSW, Würth Solar*
5b. Microstructural characterisation of ED-CIS films	*ED-CIS with improved performance*	*CIS manufacturers using the ED method; preferably the EDF*	*is already under installation*		*UB-EME, EDF*